ATLAS NOTE

ATLAS-CONF-2015-008

19th March 2015

Study of the spin and parity of the Higgs boson in di-boson decays with the ATLAS detector

The ATLAS Collaboration

Abstract

This note presents studies of the spin, parity and Lagrangian tensor structure of the Higgs boson in the $H \to ZZ^* \to 4\ell$, $H \to WW^* \to e\nu\mu\nu$ and $H \to \gamma\gamma$ decay processes at the LHC. The investigations are based on 25 fb^{-1} of pp collision data collected by the ATLAS experiment at $\sqrt{s} = 7$ TeV and $\sqrt{s} = 8$ TeV. The Standard Model (SM) Higgs boson hypothesis, corresponding to the quantum numbers $J^P = 0^+$, is tested against several alternative spin and parity models. These include two non-SM spin-0 and spin-2 models with universal and non-universal couplings to fermions and vector bosons. The results presented here exclude all of the alternative models in favour of the SM Higgs boson hypothesis at more than 99% confidence level. The tensor structure of the HVV interaction in the spin-0 hypothesis is also investigated using the $H \to ZZ^* \to 4\ell$ and $H \to WW^* \to e\nu\mu\nu$ decays. The observed distributions of the variables sensitive to the ratios of the non-SM tensor couplings to the SM ones, $\tilde{\kappa}_{HVV}/\kappa_{\mathrm{SM}}$ and $(\tilde{\kappa}_{AVV}/\kappa_{\mathrm{SM}}) \cdot \tan\alpha$, are compatible with the SM prediction. Assuming that the values of the $\tilde{\kappa}_{HVV}/\kappa_{\mathrm{SM}}$ and $(\tilde{\kappa}_{AVV}/\kappa_{\mathrm{SM}}) \cdot \tan\alpha$ couplings are the same for the HWW and HZZ processes, values of the non-SM couplings outside the intervals $-0.73 < \tilde{\kappa}_{HVV}/\kappa_{\mathrm{SM}} < 0.63$ and $-2.18 < (\tilde{\kappa}_{AVV}/\kappa_{\mathrm{SM}}) \cdot \tan\alpha < 0.83$ are excluded at 95% confidence level.

ATLAS-CONF-2015-008
19 March 2015

1 Introduction

The discovery of a Higgs boson by the ATLAS and CMS experiments [1, 2] at the Large Hadron Collider at CERN marked the beginning of a new era of experimental studies of the properties of this new particle. In the Standard Model (SM), the Higgs boson is a CP-even scalar particle, $J^{CP} = 0^{++}$ [1]. Determination of the Higgs boson spin and CP quantum numbers by the ATLAS and CMS Collaborations are reported in Refs. [3] and [4]. These studies indicate the compatibility of the observed Higgs boson spin and CP properties with SM predictions. The ATLAS measurement excluded several alternative spin and parity hypotheses in favour of quantum numbers predicted by the SM. In addition to excluding several non-SM spin hypotheses, the CMS measurement probed the tensor structure of the Higgs boson decay to SM vector bosons in the spin-0 scenario.

Theories beyond the SM (BSM) often require an extended Higgs sector featuring several neutral Higgs bosons. In such cases these bosons may be subject to CP-mixing resulting in signatures observable through the kinematics of final state particles produced in their decays [5, 6].

This note complements the ATLAS study of the Higgs boson spin and parity published in Ref. [3]. The new study takes advantage of improvements to the analysis strategy and to the modelling used to describe alternative spin hypotheses, and includes CP-mixing results for the spin-0 hypothesis. The improved modelling is based on the Higgs-boson characterisation model described in Refs. [6, 7].

The study of the spin and parity properties of the Higgs boson presented in this note is based on the $H \to \gamma\gamma$, $H \to ZZ^* \to 4\ell$ and $H \to WW^* \to e\nu\mu\nu$ decay channels and their combination. The $H \to WW^* \to e\nu\mu\nu$ analysis is described in detail in a separate publication [8]. These analyses are based on 25 fb^{-1} of pp collisions collected by the ATLAS experiment at centre-of-mass energies of 7 TeV and 8 TeV. The Standard Model hypothesis $J^P = 0^+$ is compared to alternative spin-0 models: a pseudo-scalar boson $J^P = 0^-$ and a BSM scalar boson $J^P = 0^+_h$ [9], which describes the interaction of the Higgs boson with the SM vectors bosons with higher order operators discussed in Section 3.1. Graviton-like tensor models of $J^P = 2^+$ with universal and non-universal couplings are also considered [10]. In the fixed spin and parity hypothesis test it is assumed that the resonance decay involves only one CP eigenstate.

In addition to the fixed hypothesis test, in part already performed in Ref. [3], the possible presence of BSM terms in the HVV decay [2] of the spin-0 resonance is also investigated, assuming that the resonance HVV decay involves only one CP eigenstate. The HVV interaction is described in terms of an effective Lagrangian that contains BSM CP-odd and CP-even terms [6, 7]. The relative fractions of the CP-odd and of the CP-even BSM contributions to the observed Higgs boson decays are constrained and limits on the corresponding BSM tensor couplings are derived.

This paper is organised as follows. In Section 2, the description of the ATLAS detector is given. In Section 3 the theoretical motivation is summarised, and the spin and parity models considered as well as the mixing parametrisation used to describe the HVV coupling tensor structure are discussed. In Section 4 the choice of Monte Carlo generators for the simulation of signal and backgrounds is described. The analyses of fixed spin and parity hypotheses for the three decay channels and their combination are presented in Section 5. Individual and combined studies of the tensor structure of the HVV interaction are presented in Section 6. Concluding remarks are given in Section 7.

[1] In the following, for brevity, only the J^P label is used to indicate the spin and CP quantum numbers.

[2] In tis paper the symbol V is used to describe a generic massive SM vector boson, namely the W or the Z bosons.

2 The ATLAS detector

The ATLAS detector is described in detail in Ref. [11]. ATLAS is a multipurpose detector with a forward-backward symmetric cylindrical geometry. It uses a right-handed coordinate system with its origin at the nominal interaction point (IP) in the centre of the detector and the z-axis along the beam pipe. The x-axis points from the IP to the centre of the LHC ring, and the y-axis points upward. Cylindrical coordinates (r, ϕ) are used in the transverse plane, ϕ being the azimuthal angle around the beam pipe. The pseudo-rapidity is defined in terms of the polar angle θ as $\eta = -\ln\tan\frac{\theta}{2}$.

At small radii, the inner detector (ID), immersed in a 2 T magnetic field produced by a thin superconducting solenoid located in front of the calorimeter, is made up of fine-granularity pixel and microstrip detectors. These silicon-based detectors cover the pseudo-rapidity range $|\eta| < 2.5$. A gas-filled straw-tube transition radiation tracker (TRT) complements the silicon tracker at larger radii and also provides electron identification based on transition radiation. The electromagnetic (EM) calorimeter is a lead/liquid-argon sampling calorimeter with accordion geometry. The calorimeter is divided into a barrel section covering $|\eta| < 1.475$ and two end-cap sections covering $1.375 < |\eta| < 3.2$. For $|\eta| < 2.5$ it is divided into three layers in depth, which are finely segmented in η and ϕ. An additional thin presampler layer, covering $|\eta| < 1.8$, is used to correct for fluctuations in upstream energy losses. Hadronic calorimetry in the region $|\eta| < 1.7$ uses steel absorbers and scintillator tiles as the active medium. Liquid argon calorimetry with copper absorbers is used in the hadronic end-cap calorimeters, which cover the region $1.5 < |\eta| < 3.2$. A forward calorimeter using copper or tungsten absorbers with liquid argon completes the calorimeter coverage up to $|\eta| = 4.9$. The muon spectrometer (MS) measures the deflection of muon tracks with $|\eta| < 2.7$, using three stations of precision drift tubes, with cathode strip chambers in the innermost layer for $|\eta| > 2.0$. The deflection is provided by a toroidal magnetic field with an integral of approximately 3 T-m and 6 T-m in the central and end-cap regions of the ATLAS detector, respectively. The muon spectrometer is also instrumented with separate trigger chambers covering $|\eta| < 2.4$.

3 Theoretical models

In this section, the theoretical framework for measurements of the spin and parity of the resonance is discussed. An effective field theory (EFT) approach is adopted in this note in order to describe the interactions between the resonance and the SM vector bosons, following the Higgs boson characterisation model described in Refs. [6] and [7]. Three possible scenarios for the spin and parity of the boson are considered: the hypothesis that the observed resonance is a spin-2 resonance, a pure spin-0 CP-even or CP-odd BSM Higgs boson, or a mixture of spin-0 CP-even and CP-odd states. The latter case would imply CP-violation in the Higgs sector. In the case of CP mixing, the Higgs boson would be a mass eigenstate, but not a CP eigenstate. In all cases, only one resonance with a mass of about 125 GeV is considered. It is also assumed that the total width of the resonance is small with respect to the typical experimental resolution of the ATLAS detector (of the order of 1-2 GeV in the four-lepton and $\gamma\gamma$ final states) and the interference effects between the signal and SM backgrounds are neglected.

The approach used by the Higgs boson characterisation model relies on an EFT, which by definition is only valid up to a certain energy scale, Λ. The model described in Ref [7] assumes that the resonance structure corresponds to one new boson ($X(J^P)$ with $J = 0^{\pm}, 1^{\pm}$ or 2^+), assuming that any other BSM particle exists at an energy scale larger than Λ. The case where the observed resonance has $J^P = 1^{\pm}$ is not studied in this note. The observation of the $H \to \gamma\gamma$ decay, if assumed to be produced by the resonance

studied in this note, is forbidden by the Landau–Yang theorem [12, 13] for a spin-1 particle. Moreover, the spin-1 hypothesis was already studied in the previous ATLAS publication [3] in the $H \to ZZ^* \to 4\ell$ and $H \to WW^* \to e\nu\mu\nu$ decays and excluded at more than 99% CL. The Λ cutoff scale is set to 1 TeV in this note to account for the experimental results obtained by the LHC and previous collider experiments that show no evidence of new physics at lower energy scales.

3.1 The spin-0 hypothesis

In the spin-0 hypothesis, models with fixed spin and parity, and models with mixed SM spin-0 and BSM spin-0 CP-even and CP-odd contributions are considered. In the Higgs boson characterisation model, the description of the spin-0 particle interaction with pairs of W and Z bosons is given through the following interaction Lagrangian:

$$\begin{aligned}\mathcal{L}_0^V = & \left\{ c_\alpha \kappa_{\rm SM} \left[\tfrac{1}{2} g_{HZZ} Z_\mu Z^\mu + g_{HWW} W^+_\mu W^{-\mu} \right] \right. \\ & -\tfrac{1}{4}\tfrac{1}{\Lambda} \left[c_\alpha \kappa_{HZZ} Z_{\mu\nu} Z^{\mu\nu} + s_\alpha \kappa_{AZZ} Z_{\mu\nu} \tilde{Z}^{\mu\nu} \right] \\ & \left. -\tfrac{1}{2}\tfrac{1}{\Lambda} \left[c_\alpha \kappa_{HWW} W^+_{\mu\nu} W^{-\mu\nu} + s_\alpha \kappa_{AWW} W^+_{\mu\nu} \tilde{W}^{-\mu\nu} \right] \right\} X_0 .\end{aligned} \tag{1}$$

Here V^μ represents the vector-boson field ($V = Z, W^\pm$), the $V^{\mu\nu}$ are the reduced field tensors and the dual tensor is defined as $\tilde{V}^{\mu\nu} = \frac{1}{2}\varepsilon^{\mu\nu\rho\sigma} V_{\rho\sigma}$. The symbols $\kappa_{\rm SM}$, κ_{HVV} and κ_{AVV} denote the coupling constants corresponding to the interaction of Standard Model, BSM CP-even and BSM CP-odd spin-0 particles, represented by the X_0 field, with ZZ or WW pairs. Other higher-order operators described in Ref. [7], namely the derivative operators, are not included in Eq. 1 and have been neglected in this analysis since they induce modifications of the discriminant variables well below the sensitivity achievable with the available data sample. To ensure that the Lagrangian terms are Hermitian, these couplings are assumed to be real. The mixing angle α allows for production of CP-mixed states and implies CP-violation for $\alpha \neq 0$ and $\alpha \neq \pi$, provided the corresponding coupling constants are non-vanishing. The following notation is used: $s_\alpha = \sin\alpha$ and $c_\alpha = \cos\alpha$. The Standard Model coupling strengths, g_{HVV}, are proportional to the square of the vector boson masses: $g_{HVV} \propto m^2_{Z/W}$.

In the spin-0 hypothesis, the Standard Model Higgs boson model is compared to two alternatives: the CP-odd $J^P = 0^-$ and the BSM CP-even $J^P = 0^+_h$ hypotheses. All three models are obtained by selecting the corresponding parts of the Lagrangian described in Eq. 1 while setting all other contributions to zero. The choice of couplings used for modelling the spin-0 hypotheses tested in the current analysis is shown in Table 1.

J^P	Model	Choice of tensor couplings			
		$\kappa_{\rm SM}$	κ_{HVV}	κ_{AVV}	α
0^+	Standard Model Higgs boson	1	0	0	0
0^+_h	BSM spin-0 CP-even	0	1	0	0
0^-	BSM spin-0 CP-odd	0	0	1	$\pi/2$

Table 1: Benchmark scenarios for spin-0 boson tensor couplings used in the fixed spin and parity model tests.

The investigation of the tensor structure of the HVV interaction is based on the assumption that the observed resonance has spin equal to zero. Following the parametrisation defined in Eq. 1, scenarios

where only one CP-odd or one CP-even BSM contributions at a time is present in addition to the Standard Model contribution are considered. To quantify the presence of BSM contributions in experimentally observed $H \to ZZ^*$ and $H \to WW^*$ decays, the observed ratios of couplings $(\tilde{\kappa}_{AVV}/\kappa_{\mathrm{SM}}) \cdot \tan\alpha$ and $\tilde{\kappa}_{HVV}/\kappa_{\mathrm{SM}}$ are measured for the CP-mixing and anomalous CP-even contribution scenarios, respectively. Here $\tilde{\kappa}_{AVV}$ and $\tilde{\kappa}_{HVV}$ are defined as follows:

$$\tilde{\kappa}_{AVV} = \frac{1}{4}\frac{v}{\Lambda}\kappa_{AVV} \quad \text{and} \quad \tilde{\kappa}_{HVV} = \frac{1}{4}\frac{v}{\Lambda}\kappa_{HVV}, \tag{2}$$

where v is the SM Higgs field vacuum expectation value [14].

The mixing parameters $(\tilde{\kappa}_{AVV}/\kappa_{\mathrm{SM}}) \cdot \tan\alpha$ and $\tilde{\kappa}_{HVV}/\kappa_{\mathrm{SM}}$ correspond to the ratios of tensor couplings g_4/g_1 and g_2/g_1 proposed in the anomalous couplings approach described in Ref. [9]. To compare the exclusion limits obtained in this analysis to other existing studies, the final results are also expressed in terms of effective cross-section fractions (f_{g2}, ϕ_{g2}) and (f_{g4}, ϕ_{g4}) proposed in Ref. [6] and [9]. Further details of these conversions are given in Appendix A.

The BSM terms described in Eq. 1 are also expected to change the relative contributions of the vector-boson fusion (VBF) and vector-boson associated production (VH) processes with respect to the gluon-fusion (ggF) production process, which is predicted to be the main production mode for the SM Higgs boson at the LHC. For large values of the BSM couplings, the VBF production mode can have a cross section that is comparable to ggF the process [10]. This study aims to use only kinematic properties from $H \to VV$ decays to derive information on the CP nature of the Higgs boson. The use of the signal rate information for different production modes, in the context of the EFT analysis, may increase the sensitivity to the BSM couplings at a cost of a loss in generality. In the studies presented in this note the predictions of the signal rates are not used to constraint the BSM couplings.

As described in Section 6.2, only events in the 0-jet category are used in the $H \to WW^* \to e\nu\mu\nu$ analysis for the tensor structure studies, hence this analysis has little sensitivity to the VBF production mode. The $H \to ZZ^* \to 4\ell$ analysis also has little sensitivity to the production mode since it is mainly based on variables related to the four-lepton kinematics. The Boosted Decision Tree variable used to disentangle the signal from the ZZ^* background, described in Section 6.3, includes the transverse momentum of the four-lepton system. An enhancement of the VBF production mode would improve the separation between background and signal since the transverse momentum spectrum is harder for VBF produced events than for gluon-fusion produced events. Neglecting this information for this analysis thus gives more conservative results.

3.2 The spin-2 hypothesis

In the Higgs boson characterisation model, the description of the interaction of a spin-2 particle with fermions and vector bosons is defined through the following Lagrangian:

$$\mathcal{L}_2 = \frac{1}{\Lambda}\left[\sum_V \kappa_V X^{\mu\nu}\mathcal{T}^V_{\mu\nu} + \sum_f \kappa_f X^{\mu\nu}\mathcal{T}^f_{\mu\nu}\right]. \tag{3}$$

The spin-2 tensor field $X^{\mu\nu}$ interacts with the energy-momentum tensors, $\mathcal{T}^V_{\mu\nu}$ and $\mathcal{T}^f_{\mu\nu}$, of any vector boson V and fermion f, as inspired by gravitation. The strength of each interaction is measured by the couplings κ_V, κ_f. In the simplest formulation, all couplings are equal. This scenario will be denoted hereafter as

the universal couplings scenario (UC), while scenarios with different values of the couplings are referred to as non-universal couplings (non-UC). In the UC scenario, the main production mechanism for a such a spin-2 particle X is $gg \to X$, $gq, g\bar{q} \to X$ and $q\bar{q} \to X$, hereafter referred to as QCD production. Production through electroweak processes is expected to be negligible: $\sigma_{\mathrm{EW}}/\sigma_{\mathrm{QCD}} \simeq 0.03\%$.

The simplest production processes, $gg \to X$ and $q\bar{q} \to X$, yield different polarisation states for X, hence different angular distributions of its decay products. These mechanisms are considered in the model of a graviton-like tensor with minimal couplings proposed in Ref. [9] and experimentally studied in Ref. [3]. The EFT Lagrangian, however, also allows more complex processes with emission of one or more additional partons. These, together with the presence of four-leg diagrams like $qqgX$, effectively change the polarisation states and induce angular distributions that are less easy to separate from the ones expected for a scalar resonance.

Typical UC models predicts a branching ratio of $\sim 5.1\%$ to photon pairs and negligible branching ratios to massive EW gauge bosons WW^* and ZZ^*. This prediction is disfavoured by experimental measurements, and some of the assumptions on the couplings κ should therefore be relaxed. The production of a spin-2 particle via parton collisions (gg, qg, qq initial states) is driven by the values of the couplings κ_g, κ_q, where q refers to light quarks. These couplings will be collectively referred to as QCD couplings hereafter. Presently, there are no experimental constraints on the ratio κ_q/κ_g from observed decay modes, since the separation of jets initiated by gluons or by light quarks is experimentally difficult and has not yet been attempted. The ratio κ_q/κ_g can thus be regarded as a free parameter of the model. When $\kappa_q \neq \kappa_g$, the spin-2 model acquires a unitarity-violating behaviour, as described in Section 4.1 of Ref. [7]. A striking consequence is an enhanced non QCD-like tail in the distribution of the resonance transverse momentum, p_{T}^X, of the spin-2 particle. Such a high-p_{T}^X tail is not present for the $\kappa_q = \kappa_g$ (UC) case. As stated before, however, the EFTs are valid only up to some energy scale, Λ. At higher energies, new physics phenomena are expected to enter to regularise anomalous ultra-violet behaviours. From present observations, QCD processes do not exhibit deviations from the SM up to energies higher than the TeV scale. It is therefore assumed that the scale of new physics is $\Lambda > 1$ TeV.

In the present analysis, a cut-off $p_{\mathrm{T}}^X < 300$ GeV is applied to the observed data when dealing with non-UC scenarios $\kappa_q \neq \kappa_g$. In addition, for the non-UC scenarios, a smaller cut-off $p_{\mathrm{T}}^X < 125$ GeV is also tested. This is a conservative choice for the cut-off, as the EFT must describe the physics up to the mass of the observed resonance. The choice of the cut-off does not affect the results for the UC scenario.

Despite the p_{T}^X cut-off, not all κ_q/κ_g ratios are viable. Some still produce high-p_{T}^X tails incompatible with the observed differential distribution [15].

Choice of QCD couplings		p_{T}^X cut-off (GeV)	
$\kappa_q = \kappa_g$	Universal couplings	–	–
$\kappa_q = 0$	Low light-quark fraction	300	125
$\kappa_q = 2\kappa_g$	Low gluon fraction	300	125

Table 2: Different choices of QCD couplings for the spin-2 benchmark scenarios. The values of the p_{T}^X cut-off are also shown for each case.

The spin-2 scenarios considered in this study are presented in Table 2. These models are studied in $\gamma\gamma$, WW^* and ZZ^* decay modes. The $\kappa_q = 0$ case implies a negligible coupling to light quarks as for the SM Higgs particle, whereas the $\kappa_q = 2\kappa_g$ case is an alternative scenario with an enhanced coupling to

quarks. These three benchmark models have been chosen to maximise the investigated range in the κ_q/κ_g ratio. Larger values of κ_q/κ_g with respect to the chosen benchmark would lead to very hard p_{T} spectra of the di-boson system. They are therefore easily excluded by the observed p_{T} distributions reported in Refs. [15, 16].

For the non-UC scenarios, a smaller cut-off $p_{\mathrm{T}}^{X} < 125$ GeV is also tested. This is the most conservative choice for the cut-off, as the EFT must describe the physics up to the mass of the observed resonance. The choice of the cut-off does not affect the results for the UC scenario.

In the non-UC scenarios, the contributions from EW production may in principle become sizeable. However, simulations based on the Lagrangian in Eq. 3 show that EW production of the spin-2 resonance would occur mainly in association with a massive EW bosons W, Z. From present observations, such final states are rare, suggesting that σ_{EW} could be much smaller than σ_{QCD}, and therefore they are neglected in the present analysis.

4 Data and simulated samples

The data presented in this paper were recorded by the ATLAS detector during the 2012 LHC run with proton-proton collisions at a centre-of-mass energy of 8 TeV, and correspond to an integrated luminosity of 20.3 fb^{-1}. For the $H \to \gamma\gamma$ and $H \to ZZ^* \to 4\ell$ channels, the data collected at a centre-of-mass energy of 7 TeV corresponding to an integrated luminosity of 4.5 fb^{-1} were also used. Data quality requirements are applied to reject events recorded when the relevant detector components were not operating correctly. More than 90% of the delivered luminosity is used in these studies.

For the $H \to ZZ^* \to 4\ell$ and $H \to WW^* \to e\nu\mu\nu$ analyses the Monte Carlo (MC) simulated samples for the backgrounds and the SM Higgs boson signal are the same as the ones used for the analysis described in Refs. [17, 18], with the exception of the non-SM signal samples. An overview of the signal samples is given in Section 4.1, while background samples are briefly described in Section 4.2

The effects of the underlying event and of additional minimum bias interactions occurring in the same or neighbouring bunch crossings, and referred to as pile-up in the following, are modelled with Pythia 8 [19], and the ATLAS detector response is simulated [20] using either Geant 4 [21] or Geant 4 combined with a parametrised Geant 4-based calorimeter simulation [22].

4.1 SM Higgs boson and BSM signal samples

The SM Higgs boson signal production for all analyses is modelled using Powheg [23] generator at next-to-leading order, interfaced to Pythia 8 for parton showering and hadronisation, and for multi-parton interactions. To improve the modelling of the SM Higgs-boson p_{T}, a reweighting procedure is applied. This procedure applies to each event a weight depending on the Higgs-boson p_{T} in order to reproduce the prediction of the next-to-next-to-leading order (NNLO) and next-to-next-to-leading logarithms (NNLL) dynamic-scale calculation given by the hres2.1 program [24, 25].

For the $H \to \gamma\gamma$ analysis the signal samples are generated at several values of the Higgs boson mass m_H around 125 GeV. Then all signal yields and diphoton-mass shape parameters (both inclusively and for each category in the analysis) are parametrised as continuous functions of m_H. The spin-2 samples are generated using the MadGraph5_aMC@NLO [10] MC with LO accuracy for 0, 1, 2 additional partons,

and subsequently matched to a model of the parton shower, underlying event and hadronisation, using Pythia 6 [26].

In the $H \to ZZ^* \to 4\ell$ analysis the signal samples representing the production and decay of Higgs bosons with spin-0 and different parities are generated in the following way. The SM Higgs boson production via gluon-fusion at the mass $m_H = 125.5$ GeV is simulated using the Powheg Monte-Carlo [23] generator. For the non-SM signals, the decay of the generated Higgs bosons are then simulated, according to the Higgs boson parity assumptions, using the JHU MC [9] generator at leading order. The spin-2 samples are generated using MadGraph5_aMC@NLO [10] MC generator, as for the $H \to \gamma\gamma$ analysis.

For the $H \to WW^* \to e\nu\mu\nu$ analysis the SM Higgs-boson signal is generated at $m_H = 125$ GeV. The spin-0 BSM signal benchmarks are generated using MadGraph5_aMC@NLO [10]. The signal samples representing the production and decay of Higgs bosons with spin-2 are generated using the MadGraph5_aMC@NLO [10] MC generator, as for the $H \to \gamma\gamma$ analysis.

For studies of the tensor structure of the HVV decay, all simulated signal samples are obtained by using the matrix element (ME) reweighting method applied to a CP-mixed sample. This provides a description of different CP-mixing configurations. The reweighting procedure is validated against samples produced at different values of the couplings, to ensure that the distributions of the CP-sensitive final state observables and of their correlations are reproduced correctly. For the $H \to ZZ^* \to 4\ell$ analysis, the MC production is only performed for one set of tensor couplings: $g_1 = 1$, $g_2 = 1 + i$, $g_4 = 1 + i$ [27]. All other configurations of couplings are obtained by reweighting this base sample at generator level. The ratios of the corresponding squares of ME calculated at LO are used as weights. To calculate these ME, the JHUGenME [27] program is used. In the $H \to WW^* \to e\nu\mu\nu$ analysis only one MC sample is generated using MadGraph5_aMC@NLO with parameters $\kappa_{SM} = 1, \kappa_{AWW} = 2, \kappa_{HWW} = 2, c_\alpha = 0.3$, and all other samples are obtained from it by reweighting the events on the basis of the ME amplitudes.

4.2 Background samples

For the $H \to ZZ^* \to 4\ell$, $H \to WW^* \to e\nu\mu\nu$ and $H \to \gamma\gamma$ analyses, the MC simulated samples for the backgrounds and the corresponding cross-sections calculations are the same as the ones adopted for the analyses described in Refs [17, 18, 28], respectively. In the $H \to \gamma\gamma$ analysis the background is dominated by prompt $\gamma\gamma$ events, with smaller contributions from γ-jet events. For the $H \to ZZ^* \to 4\ell$ analysis the major background is the non-resonant ZZ^* process, with minor contributions from the $t\bar{t}$ and Z+jets processes. For the $H \to WW^* \to e\nu\mu\nu$ analysis the dominant backgrounds are the non-resonant W boson pair (WW) production, the $t\bar{t}$ and single-top quark production and the Z/γ^* process, followed by the decay to $\tau\tau$ final states.

5 Fixed spin and parity hypotheses test

In the following, the analyses used for the fixed spin and parity hypothesis tests are described. The $H \to \gamma\gamma$ and $H \to ZZ^* \to 4\ell$ analyses are improved with respect to the previous ATLAS publication of Ref. [3]. These analyses are described in detail in the following subsections. The spin and parity analysis in the $H \to WW^* \to e\nu\mu\nu$ channel has also been improved. It is discussed in detail in a separate publication [8]. In the following only a brief overview of this analysis is given. The expected and observed results of the individual channels and in their combination are presented in the Section 5.5.

5.1 Statistical treatment

The analyses described in this paper rely on discriminant observables chosen to be sensitive to the spin and parity of the signal while preserving the discrimination against the various backgrounds as described in the following sections.

A likelihood function $\mathcal{L}(J^P, \mu, \vec{\theta})$ that depends on the spin-parity assumption of the signal is constructed as a product of conditional probabilities over binned distributions of the discriminant observables in each channel:

$$\mathcal{L}(\text{data} \mid J^P, \mu, \vec{\theta}) = \prod_{j}^{N_{\text{chann.}}} \prod_{i}^{N_{\text{bins}}} P(N_{i,j} \mid \mu_j \cdot S_{i,j}^{(J^P)}(\vec{\theta}) + B_{i,j}(\vec{\theta})) \times \mathcal{A}_j(\vec{\theta}) \,, \tag{4}$$

where μ_j represents the parameter associated with the signal rate normalised to the SM prediction in each channel j. [3] The signal rates are treated as independent parameters for each decay channel and between different LHC centre-of-mass energies, as discussed in Section 3. The symbol $\vec{\theta}$ represents all nuisance parameters. The likelihood function is a product of Poisson distributions P corresponding to the observation of $N_{i,j}$ events in each bin i of the discriminant observable(s)[4], given the expectations for the signal, $S_{i,j}^{(J^P)}(\vec{\theta})$, and for the background, $B_{i,j}(\vec{\theta})$. Some of the nuisance parameters are constrained by auxiliary measurements. Corresponding constraints are represented by the functions $\mathcal{A}_j(\vec{\theta})$.

While for the SM Higgs boson the couplings to the SM particles are predicted, they are not known *a priori* for the alternative hypotheses, defined as J^P_{alt}. In order to be insensitive to assumptions on alternative hypotheses couplings to SM particles, the numbers of signal events in each channel and for each tested hypothesis are treated as independent parameters in the likelihood and fitted to the data when deriving limits on the spin and parity hypothesis.

The test statistic q used to distinguish between the two signal spin-parity hypotheses is based on a ratio of profiled likelihoods [29]:

$$q = \log \frac{\mathcal{L}(J^P_{\text{SM}}, \hat{\hat{\mu}}_{J^P_{\text{SM}}}, \hat{\hat{\theta}}_{J^P_{\text{SM}}})}{\mathcal{L}(J^P_{\text{alt}}, \hat{\hat{\mu}}_{J^P_{\text{alt}}}, \hat{\hat{\theta}}_{J^P_{\text{alt}}})} \,, \tag{5}$$

where $\mathcal{L}(J^P, \hat{\hat{\mu}}_{J^P}, \hat{\hat{\theta}}_{J^P})$ is the maximum likelihood estimator, evaluated under either the SM $J^P_{\text{SM}} = 0^+$ or the J^P_{alt} spin-parity hypothesis. The $\hat{\hat{\mu}}_{J^P}$, $\hat{\hat{\theta}}_{J^P}$ represent the values of the signal strength and nuisance parameters fitted to the data under each J^P hypothesis. The distributions of the test statistic for both the J^P_{SM} and the J^P_{alt} hypotheses are obtained using ensemble tests (Monte Carlo pseudo-experiments). The generation of the pseudo-experiments uses the numbers of signal and background events in each channel obtained from maximum likelihood fits to data. In the fits of each pseudo-experiment, these and all other nuisance parameters are profiled, i.e. fitted to the value that maximises the likelihood for each value of the parameter of interest. When generating the distributions of the test statistic for a given spin-parity hypothesis, the signal strength μ is fixed to the value obtained in the fit to the data under the

[3] Here channel can be used to indicate different categories in the same final state when producing individual decay channel results, or different final states when combining them.

[4] As explained in the following sections, the sensitivity for spin-parity separation is improved by a simultaneous fit to two discriminants in the $H \to \gamma\gamma$ and $H \to WW^* \to e\nu\mu\nu$ decay modes, while in the $H \to ZZ^* \to 4\ell$ channel only one discriminant is used.

same spin-parity assumption. The distributions of q are used to determine the corresponding p-values $p(J^P_{\rm SM}) = p^{SM}$ and $p(J^P_{\rm alt}) = p^{ALT}$. For a tested hypothesis $J^P_{\rm alt}$, the observed (expected) p-values are obtained by integrating the corresponding test-statistic distributions above the observed value of q (above the median of the $J^P_{\rm SM}$ q distribution). When the measured data are in agreement with the tested hypothesis, the observed value of q is distributed such that all p-values are equally probable. For each hypothesis test, about 70 thousand pseudo-experiments have been generated.

Very small values of the integral of the $J^P_{\rm alt}$ distribution, corresponding to large values of q, are interpreted as the data being in disagreement with the tested hypothesis in favour of the SM hypothesis.

The exclusion of the alternative $J^P_{\rm alt}$ hypothesis in favour of the SM $J^P_{\rm SM}$ hypothesis is evaluated in terms of the corresponding $\mathrm{CL_s}(J^P_{\rm alt})$, defined as [30]:

$$\mathrm{CL_s}(J^P_{\rm alt}) = \frac{p(J^P_{\rm alt})}{1 - p(J^P_{\rm SM})} \,. \tag{6}$$

5.2 Spin analysis in the $H \to \gamma\gamma$ channel

The selection of $H \to \gamma\gamma$ candidate events is based on that of the other ATLAS $H \to \gamma\gamma$ analyses (see e.g. Ref. [28]). Data are selected if they pass a diphoton trigger requiring loose identification criteria, with $p_{\rm T}$ thresholds of 35 GeV and 25 GeV for the leading and sub-leading photons, respectively. During the offline selection two photons are further required to be in a fiducial pseudo-rapidity region, defined by $|\eta^\gamma| < 2.37$, where the barrel-endcap transition region $|\eta^\gamma| \in [1.37; 1.56]$ is excluded. Their transverse momenta must satisfy $p_{\rm T}^{\gamma 1} > 0.35\, m_{\gamma\gamma}$ and $p_{\rm T}^{\gamma 2} > 0.25\, m_{\gamma\gamma}$, respectively, and only the events with invariant mass $m_{\gamma\gamma}$ between 105 and 169 GeV are retained. For diphoton events passing this selection, a further requirement is applied on the diphoton transverse momentum, $p_{\rm T}^{\gamma\gamma} < 300$ GeV, motivated by the assumed validity limit of the spin-2 EFT model, as explained in Section 3. After this selection, 17 220 events are left at $\sqrt{s} = 7$ TeV and 94 540 events at $\sqrt{s} = 8$ TeV.

The kinematic variables sensitive to the spin of the resonance are the diphoton transverse momentum $p_{\rm T}^{\gamma\gamma}$ and the production angle of the two photons, measured in the Collins-Soper frame [31]:

$$|\cos\theta^*| = \frac{|\sinh(\Delta\eta^{\gamma\gamma})|}{\sqrt{1 + (p_{\rm T}^{\gamma\gamma}/m_{\gamma\gamma})^2}} \frac{2 p_{\rm T}^{\gamma 1} p_{\rm T}^{\gamma 2}}{m_{\gamma\gamma}^2} \,, \tag{7}$$

where $\Delta\eta^{\gamma\gamma}$ is the separation in pseudo-rapidity of the two photons.

The distributions of these variables, for events passing the selection, are shown in Figure 1, for a SM Higgs boson and for a spin-2 particle with different QCD couplings. For the $\kappa_q \neq \kappa_g$ cases, the enhanced high-$p_{\rm T}^{\gamma\gamma}$ tail offers the best discrimination, whereas for $\kappa_q = \kappa_g$ the sensitive variable is $|\cos\theta^*|$.

To exploit the signal distribution both in $p_{\rm T}^{\gamma\gamma}$ and $|\cos\theta^*|$, the selected events are divided into 11 categories: 10 categories collect events with $p_{\rm T}^{\gamma\gamma} < 125$ GeV, divided in 10 equal bins of $|\cos\theta^*|$, while the 11$^{\rm th}$ category groups all events with $p_{\rm T}^{\gamma\gamma} \geq 125$ GeV. The numbers of events collected in each category are summarised in Table 3. As described in Section 3, for the non-UC spin-2 models the analysis is performed with two cut-offs $p_{\rm T}^{\gamma\gamma} < 300$ GeV and $p_{\rm T}^{\gamma\gamma} < 125$ GeV: the latter case corresponds to dropping the 11$^{\rm th}$ category.

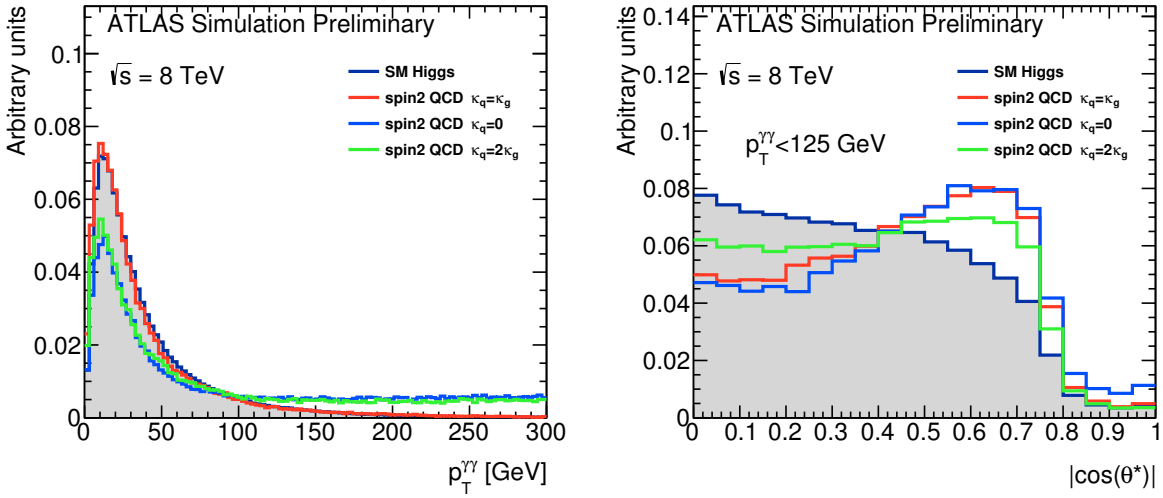

Figure 1: Expected distributions of $p_{\mathrm{T}}^{\gamma\gamma}$ (left) and $|\cos\theta^*|$ (right), for a SM Higgs boson (shaded histograms) and for spin-2 particles, for three different choices of the QCD couplings.

Name	Definition		Selected events	
			$\sqrt{s}$ = 7 TeV	$\sqrt{s}$ = 8 TeV
C1	$p_{\mathrm{T}}^{\gamma\gamma} < 125$GeV and	$0.0 \le \lvert\cos\theta^*\rvert < 0.1$	1886	10020
C2		$0.1 \le \lvert\cos\theta^*\rvert < 0.2$	1712	9514
C3		$0.2 \le \lvert\cos\theta^*\rvert < 0.3$	1766	9556
C4		$0.3 \le \lvert\cos\theta^*\rvert < 0.4$	1823	9781
C5		$0.4 \le \lvert\cos\theta^*\rvert < 0.5$	2144	11606
C6		$0.5 \le \lvert\cos\theta^*\rvert < 0.6$	2370	12875
C7		$0.6 \le \lvert\cos\theta^*\rvert < 0.7$	2729	14531
C8		$0.7 \le \lvert\cos\theta^*\rvert < 0.8$	2050	12116
C9		$0.8 \le \lvert\cos\theta^*\rvert < 0.9$	302	1860
C10		$0.9 \le \lvert\cos\theta^*\rvert < 1.0$	179	1185
C11	125 GeV $\le p_{\mathrm{T}}^{\gamma\gamma} <$ 300 GeV		259	1496
Total			17220	94540

Table 3: Definitions of categories in the $H \to \gamma\gamma$ analysis and the number of selected events.

In each category, the numbers of signal events over the continuum background can be estimated through a fit to the observed $m_{\gamma\gamma}$ distribution. The latter is modelled in each category as a the sum of 1-dimensional probability density functions (pdf) for signal and background distributions:

$$f^{[c]}(m_{\gamma\gamma}|J) = \frac{n_B^{[c]} f_B^{[c]}(m_{\gamma\gamma}) + (n_J^{[c]} + n_{bias}^{[c]}) f_S^{[c]}(m_{\gamma\gamma})}{n_B^{[c]} + n_J^{[c]} + n_{bias}^{[c]}}, \tag{8}$$

where J is the spin hypothesis (SM Higgs boson, or any of the spin-2 models), $n_B^{[c]}$ and $n_J^{[c]}$ are the background and the signal yield in category c, and $f_B^{[c]}(m_{\gamma\gamma})$, $f_S^{[c]}(m_{\gamma\gamma})$ are the $m_{\gamma\gamma}$ pdfs for the background and the signal, respectively. The signal pdf $f_S^{[c]}(m_{\gamma\gamma})$ is modelled as a weighted sum of a Crystal-Ball function, describing the core and the lower tail, and of a Gaussian component that improves the description of the upper tail. For each category, $f_S^{[c]}(m_{\gamma\gamma})$ is fitted to the simulated $m_{\gamma\gamma}$ distribution of the SM Higgs boson, and verified to be consistent also with the spin-2 models. The assumed value for the mass of the resonance is $m_X = 125.4$ GeV, from the combined ATLAS measurement of the mass of the Higgs boson [32]. The background pdf $f_B^{[c]}(m_{\gamma\gamma})$ is empirically modelled as an exponential of a 1st or 2nd degree polynomial. The choice of such a parametrisation can induce a bias ("spurious signal") on the fitted signal yield, which is accounted for by the term $n_{bias}^{[c]}$. Its size is determined as described in Refs. [15, 28], and ranges between 0.6 and 4 events, depending on the category. In the statistical analysis, for each category $n_{bias}^{[c]}$ is constrained by multiplying the likelihood function by a Gaussian function centred in zero and with width determined by the size of the bias.

Defining n_S as the total signal yield (summed over all categories), the fraction of signal events per category, $\Phi_J^{[c]} \equiv \dfrac{n_J^{[c]}}{n_S}$ depends on the spin hypothesis J. The values of $\Phi_J^{[c]}$ extracted from the data can be compared to their expected values for each spin hypotheses, as shown in Figure 2 (left) for $\sqrt{s} = 8$ TeV data.

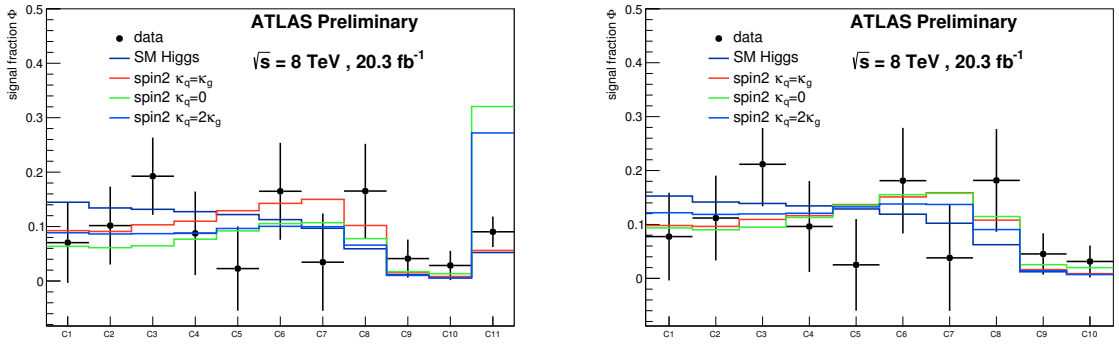

(a) $p_{\mathrm{T}}^{\gamma\gamma} < 300$ GeV

(b) $p_{\mathrm{T}}^{\gamma\gamma} < 125$ GeV

Figure 2: Observed signal fraction per category in $\sqrt{s} = 8$ TeV data, and comparison to expected values for a SM Higgs boson and for a spin-2 particle with different choices of QCD couplings: on the left, 11 categories are displayed, corresponding to the $p_{\mathrm{T}}^{\gamma\gamma} < 300$ GeV cut-off; on the right, the high-$p_{\mathrm{T}}^{\gamma\gamma}$ category is discarded and the signal fractions are renormalised over the 10 remaining categories, as for the $p_{\mathrm{T}}^{\gamma\gamma} < 125$ GeV cut-off.

For the non-UC scenario the 11$^{\mathrm{th}}$ (high-$p_{\mathrm{T}}^{\gamma\gamma}$) category provides a strong discrimination power against the SM hypothesis, as visible in (Figure 2 (left)).

To discriminate between the SM spin-0 ($J^P_{\rm SM} = 0^+$) and alternative spin-2 hypotheses ($J^P_{\rm alt}$), two likelihood functions $\mathcal{L}_{J^P_{\rm SM}}$, $\mathcal{L}_{J^P_{\rm alt}}$ are built, following the general approach descibed in Eq. 4:

$$-\ln \mathcal{L}_J = \sum_c \left\{ \left(n_B^{[c]} + n_S \Phi_J^{[c]} + n_{bias}^{[c]} \right) - \sum_{e \in [c]} \ln \left[n_B^{[c]} f_B^{[c]}(m_{\gamma\gamma}^{(e)}) + (n_S \Phi_J^{[c]} + n_{bias}^{[c]}) f_S^{[c]}(m_{\gamma\gamma}^{(e)}) \right] \right\} \tag{9}$$

where the $\sum_c$ runs over all categories and the $\sum_{e \in [c]}$ runs over all events in category c. The total signal yield n_S is a free parameter in the likelihood model. The spin hypothesis being tested enters the likelihood function through the fractions of signal per category, $\Phi_J^{[c]}$.

Several systematic uncertainties enter this model. All of them are implemented for each spin hypothesis as nuisance parameters θ_J constrained by multiplicative Gaussian terms in the likelihood function (not included in Eq. 9 for simplicity).

The signal fractions $\Phi_J^{[c]}$ for the SM Higgs boson are affected by uncertainties on the $p_{\rm T}$ spectrum of the resonance and on the size of the resonant-continuum interference. The former is computed as described in Ref. [28]. The relative impact is less than ±1% for categories 1 to 8 ($p_{\rm T}^{\gamma\gamma} < 125$ GeV and $|\cos\theta^*| < 0.8$), and becomes as large as ±13% for categories 10 and 11. The correction for the interference is evaluated both at LO and NLO according to Refs. [33, 34][5]. The systematic uncertainty is computed as the difference between "twice the correction" and "no correction", and its relative impact ranges between ±0.1% and ±1.8%.

For spin-2 models, the $p_{\rm T}$ (X) distribution from the simulation is assumed without uncertainty. The effect of the resonant-continuum interference is essentially undetermined, as it depends on the width Γ_X of the resonance, which is unknown. For a width comparable to that of a SM Higgs boson ($\Gamma_X \simeq 4$ MeV), the effect of the interference is negligible. The results presented here hold only under this assumption.

Additional systematic uncertainties come from uncertainties on the energy scale and resolution and enter the signal parametrisation $f_S^{[c]}$. They have been evaluated as described in Ref. [32].

5.3 Spin and parity analysis in the $H \to WW^* \to e\nu\mu\nu$ channel

The analysis of the spin and parity in the $H \to WW^* \to e\nu\mu\nu$ channel is described in detail in a separate publication [8]. In the following a brief summary is provided. The selection is restricted to events containing two leptons of different flavour (one electron and one muon). The leading lepton is required to have $p_{\rm T} > 22$ GeV and to match the triggering object, while the sub-leading lepton needs to have $p_{\rm T} > 15$ GeV. While the spin-0 analyses select only events with no jets in the final state (no observed jets with $p_{\rm T} > 25$ GeV within $|\eta| < 2.5$ or with $p_{\rm T} > 30$ GeV within $2.5 < |\eta| < 4.5$), the spin-2 analysis enlarges the acceptance allowing for zero or one jet (selected according to the above mentioned criteria).

The major sources of background after the dilepton selection are Z/γ^*+jets (Drell–Yan events), diboson (WW, WZ/γ^*, ZZ/γ^*), top-quark ($t\bar{t}$ and single top) production, and W bosons produced in association with hadronic jets, where a jet is misidentified as a lepton. The contribution from misidentified leptons is significantly reduced by the requirement of two high-$p_{\rm T}$ isolated leptons. Drell-Yan events are suppressed

[5] Above $|\cos\theta^*| = 0.7$ only the NLO graph is present, while below both LO and NLO contribute. In this case, the correction is effectively applied as the average (LO+NLO)/2. The motivation is that NLO introduce too large corrections, that are estimated to reduce sizably at NNLO.

through requirements on some of the dilepton variables[6] ($p_{\mathrm{T}}^{\ell\ell} > 20$ GeV, $\Delta\phi_{\ell\ell} < 2.8$), while a cut on $m_{\ell\ell}$ ($m_{\ell\ell} < 80$ GeV) targets the WW background. For alternative spin models with non-universal couplings, as discussed in Section 3, an additional upper threshold is imposed on the Higgs boson p_T, reconstructed for all simulated and real data as the transverse component of the vector sum of the two charged-leptons momenta and the missing momentum. Additionally, for events containing one jet, which are polluted by substantial top-quark and W+jets backgrounds, b-jet and $Z \to \tau^+\tau^-$ vetoes are applied, together with transverse mass requirements: the largest among the transverse masses of the two W bosons (each computed using the corresponding lepton and the missing transverse momentum) in the event is required to be larger than 50 GeV, while the total transverse mass of the WW system (defined with the two leptons and the missing momentum) is required to be below 150 GeV.

Control regions (CRs) are defined for the WW, top-quark and Drell–Yan backgrounds, which are the most important ones after the topological selection described above. The CRs are used to normalise the expected event yields in the signal region (SR) to the rates observed in the data. The W+jets background is estimated entirely from data, while non-WW diboson backgrounds are estimated using MC simulation and cross-checked in a validation region.

After the signal region selection, 4730 and 1569 candidate events are found in data in the 0-jet and 1-jet categories, respectively. For the latter case, the number decreases to 1567 and 1511 events when applying a selection on the Higgs boson p_T of < 300 GeV and < 125 GeV, respectively. In total 218 (77) events are expected from a SM Higgs boson signal in the 0-jet (1-jet) category, while about 4390 (1413) events are expected for the total background, after all normalisations.

A Boosted Decision Tree (BDT) algorithm is used in both the spin and parity analyses. For spin-2 studies, the strategy follows the one adopted in Ref. [3], with the main difference that the 1-jet channel has been added. Two BDT discriminants are trained to distinguish between the SM hypothesis and the background (BDT_0), and the alternative spin hypothesis and the background (BDT_2). Both trainings employ the same variables, namely $m_{\ell\ell}$, $p_{\mathrm{T}}^{\ell\ell}$, $\Delta\phi_{\ell\ell}$ and m_{T}, which provide the best separation between signal hypotheses and backgrounds, also in the presence of one jet in the final state. All background components are used in the trainings. In total, five BDT_2 trainings are performed for the alternative spin hypotheses, plus one for the SM Higgs boson hypothesis.

For spin-0 and HWW tensor structure studies, the first discriminant, BDT_0, is the same as the one used for the spin-2, trained to disentangle the SM hypothesis from the background; additionally, a second BDT discriminant, $\mathrm{BDT}_{\mathrm{CP}}$, is obtained by training the SM signal versus the alternative signal sample (the pure CP-even or CP-odd hypotheses, and then applied to all CP-mixing fractions. No background component is involved in this case. The variables used for the $\mathrm{BDT}_{\mathrm{CP}}$ trainings are $m_{\ell\ell}$, $\Delta\phi_{\ell\ell}$, $p_{\mathrm{T}}^{\ell\ell}$ and the missing transverse energy for the CP-even analysis, and $m_{\ell\ell}$, $\Delta\phi_{\ell\ell}$, $E_{\ell\ell\nu\nu}$ and Δp_T for the CP-odd analysis.

The training strategy is different from the one used in the spin analysis because, while the spin-2 signal is very background-like, the spin-0 signals are all similar to each other, while being different from the main background components. Therefore, in the latter case, training the signal hypotheses against each other improves the sensitivity. The resulting BDT variable is afterwards used in binned likelihood fits to test the data for compatibility with the presence of a SM or BSM Higgs boson.

[6] Throughout this section, the following variables are used: $p_{\mathrm{T}}^{\ell\ell}$, $m_{\ell\ell}$ and $\Delta\phi_{\ell\ell}$ are the transverse p_{T}, the invariant mass and the azimuthal angular difference for the two-leptons system, respectively, m_{T} is the transverse mass of the reconstructed Higgs boson decay system, Δp_T is the absolute value of the difference between leptons' momenta and $E_{\ell\ell\nu\nu} = p_{\mathrm{T}}^{\ell_1} - 0.5 p_{\mathrm{T}}^{\ell_2} + 0.5 E_{\mathrm{T}}$, where E_{T} is the transverse missing momentum.

Several sources of systematic uncertainties are considered, both from experimental and theoretical sources, and are described in detail in Ref. [8]. The correlations introduced among the different background sources by the presence of other processes in the control regions are fully taken into account in the statistical procedure. The most important systematic uncertainties are found to be those related to the modelling of the WW background, to the estimate of the W+jets background (due to the data-driven method employed) and, for the spin-2 results in particular, to the $Z \to \tau\tau$ modelling.

5.4 Spin and parity analysis in the $H \to ZZ^* \to 4\ell$ channel

The reconstruction of physics objects and event selection used for this analysis is identical to the one presented in Ref. [35]. The main elements of the event reconstruction and selection, relevant for the analysis presented in this note, are outlined in this section.

Events containing four reconstructed leptons (electrons or muons) in the final state are selected using single-lepton and di-lepton triggers. The selected events are classified according to their final state: 4μ, $2e2\mu$, $2\mu2e$ and $4e$, where for the decay modes $2e2\mu$ and $2\mu2e$ the first pair is defined to be the one with the dilepton mass closest to the Z boson mass. Each muon (electron) must satisfy p_{T} >6 GeV (E_{T} >7 GeV) and be measured in the pseudo-rapidity range $|\eta|$ <2.7 ($|\eta|$ <2.47). Higgs boson candidates are formed by selecting two same-flavour, opposite-sign lepton pairs in an event. The highest p_{T} lepton in the quadruplet must satisfy $p_{\mathrm{T}} > 20$ GeV, the second and third highest p_{T} leptons must satisfy $p_{\mathrm{T}} > 15$ GeV and p_{T} >10 GeV respectively. For each final state, the lepton pair with the mass closest to the Z boson mass is referred to as the leading lepton pair and its invariant mass as m_{12}. The requirement 50< m_{12} <106 GeV is applied. The other lepton pair is chosen from the remaining leptons as the pair closest in mass to the Z boson. Its mass, denoted hereafter as m_{34}, must satisfy 12 GeV < m_{34} <115 GeV. Further requirements are made on the leptons impact parameters and their isolation in both the the tracker and calorimeter.

The main background process affecting the selection of $H \to ZZ^* \to 4\ell$ events is the non-resonant production of ZZ^* pairs. This background has the same final state as the signal events and hereafter will be referred to as the irreducible background. It is estimated from simulation and normalised to the expected SM cross section calculated at NLO. The reducible sources of background come from Z+jets and $t\bar{t}$ processes, where additional leptons come from mis-identified jets or from t decays. The rate and composition of the reducible backgrounds are evaluated using data-driven techniques, separately for the two final states with sub-leading muons $\ell\ell + \mu\mu$ and those with sub-leading electrons $\ell\ell + ee$.

In the analysis presented in this note, only events whose four lepton system invariant mass, denoted as $m_{4\ell}$, satisfies the signal region definition 115< $m_{4\ell}$ <130 GeV are employed. The expected signal and background yields in the signal region and the observed events in data are reported in Table 4.

The choice of production and decay angles used in this analysis is presented in Figure 3, where the following definitions are used:

- θ_1 and θ_2 are defined as the angles between negative final state leptons and the direction of flight of their respective Z-bosons, in the four-lepton rest frame;
- Φ is the angle between the decay planes of four final state leptons expressed in the four-lepton rest frame;

	Signal	ZZ^*	$t\bar{t}$, Z + jets	Observed
		$\sqrt{s}$ = 7 TeV		
4μ	1.02±0.10	0.65±0.03	0.14±0.06	3
$2\mu 2e$	0.47±0.05	0.29±0.02	0.53±0.12	1
$2e2\mu$	0.64±0.06	0.45±0.02	0.13±0.05	2
$4e$	0.45±0.04	0.26±0.02	0.59±0.12	2
Total	2.58±0.25	1.65±0.09	1.39±0.26	8
		$\sqrt{s}$ = 8 TeV		
4μ	5.81±0.58	3.36±0.17	0.97±0.18	13
$2\mu 2e$	3.00±0.30	1.59±0.10	0.52±0.12	8
$2e2\mu$	3.72±0.37	2.33±0.11	0.84±0.14	9
$4e$	2.91±0.29	1.44±0.09	0.52±0.11	7
Total	15.4 ±1.5	8.72±0.47	2.85±0.39	37

Table 4: Expected signal and background yields, and observed events in data, in the $115 < m_{4\ell} < 130$ GeV signal region. The number of signal events is given for a Higgs boson mass of 125.5 GeV.

- Φ_1 is the angle defined between the decay plane of the leading lepton pair and a plane defined by the vector of the Z_1 (the Z boson associated to the leading lepton pair) in the four-lepton rest frame and the positive direction of the collision axis;
- θ^* is the production angle of the Z_1 defined in the four-lepton rest frame.

The final state observables sensitive to the parity of a boson decaying to $ZZ^* \to 4\ell$ are the two production angles θ^* and Φ_1 and the three decay angles: Φ, θ_1 and θ_2. In the case of a spin-0 boson, the differential production cross section does not depend on the production variables $\cos(\theta^*)$ and Φ_1 since the underlying resonance has no spin axis with which one can define these angles. It should be noted that as resonance mass is below 180 GeV, the shapes of the mass distributions of intermediate Z bosons, m_{12} and m_{34}, are sensitive to spin and parity of the underlying resonance. In Figure 4 the distributions of the final state observables sensitive to the spin and parity of the decaying resonance are presented. The distributions are shown for the $J^P = 0^+$ and $J^P = 0^-$ Monte Carlo events, as well as for ZZ^* and reducible backgrounds in the signal region 115 GeV $< m_{4\ell} <$ 130 GeV. The events observed in data are superimposed on each plot.

Two approaches have been pursued to develop the discriminants used to distinguish between pairs of spin and parity states. The first uses the theoretical differential decay rate for the parity sensitive final state observables, corrected for the detector acceptance and analysis selection, to construct a matrix element-based likelihood ratio analysis (J^P – MELA) that is used as a discriminant between different spin and parity hypotheses. The second approach is based on a BDT.

For the J^P – MELA approach, the probability of observing a given event kinematics can be calculated. This probability is corrected for detector acceptance and analysis selection which are obtained from the simulated signal MC samples. The full pdf also includes a term for the incorrect pairing of the leptons for the 4μ and $4e$ channels. For a given pair of spin-parity hypotheses under test, the final discriminant is defined as the ratio of the pdf of a given hypothesis divided by the sum of the pdfs of both hypotheses.

For the BDT approach, a J^P discriminant is formed for each pair of spin-parity states to be tested, by training a BDT on the variables of fully simulated signal events which fall in the signal mass window

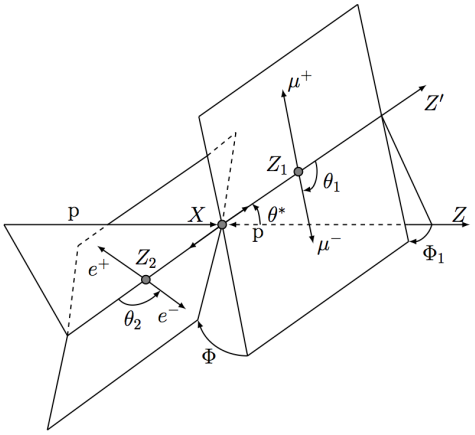

Figure 3: Definitions of angular observables sensitive to the spin and parity of the decaying resonance in $H \to ZZ^* \to 4\ell$ decay.

115 GeV $< m_{4\ell} <$ 130 GeV. For the 0^+ versus 0^- test, only the parity-sensitive observables Φ, θ_1, θ_2, m_{12} and m_{34} are used in the BDT training. For the spin-2 test, the production angles θ^* and Φ_1 are also considered.

Both analyses are complemented with a BDT discriminant designed to separate the signal from the ZZ^* background. These discriminants are hereafter referred to as BDT_{ZZ}. For the J^P – MELA analysis, the BDT_{ZZ} is fully equivalent to the one described in Ref. [35, 36]. For the BDT analysis the discriminating variables used for the background BDT_{ZZ} are: the 4-lepton system invariant mass, pseudo-rapidity and transverse momentum, and a matrix-element based kinematic discriminant K_D defined in [37]. The results from both methods are obtained from likelihood fits to the two-dimensional distributions of the background BDTs and of the spin and parity sensitive discriminants. In this way the small correlation between these variables are taken into account in the analyses. The distribution of the background discriminant BDT_{ZZ} versus the J^P – MELA discriminant is presented in Figure 5 for the $J^P = 0^+$ signal, the backgrounds, and the data.

Two general types of systematic effects impact the fixed spin and parity hypotheses analyses: the variations of discriminant shapes due to uncertainties on detector effects, and the variations of signal and background normalisations due to theory uncertainties and uncertainties on data-driven background determination methods. The shape systematic uncertainties are included in the analysis by creating discriminant shapes corresponding to one standard deviation variations of the corresponding systematic sources. The normalisation systematic uncertainties are included as additional nuisance parameters in the likelihood.

The list of systematic sources common for all ATLAS $H \to ZZ^* \to 4\ell$ analyses is presented in Ref. [17]. The impact of these sources on the final separation of all hypotheses pairs are evaluated and sources affecting the final separation (given in Section 5.5) by less than ±0.5% of its value are neglected.

In this paper only results based on the J^P-MELA approach are reported. The BDT approach was used as a cross-check and produced compatible results.

The main source of systematic uncertainties are related to the experimental error on the Higgs boson mass, the modelling of the irreducible ZZ background, the uncertainty on the total luminosity and the experimental uncertainties on the electron and muon reconstruction. For the J^P-MELA method, the

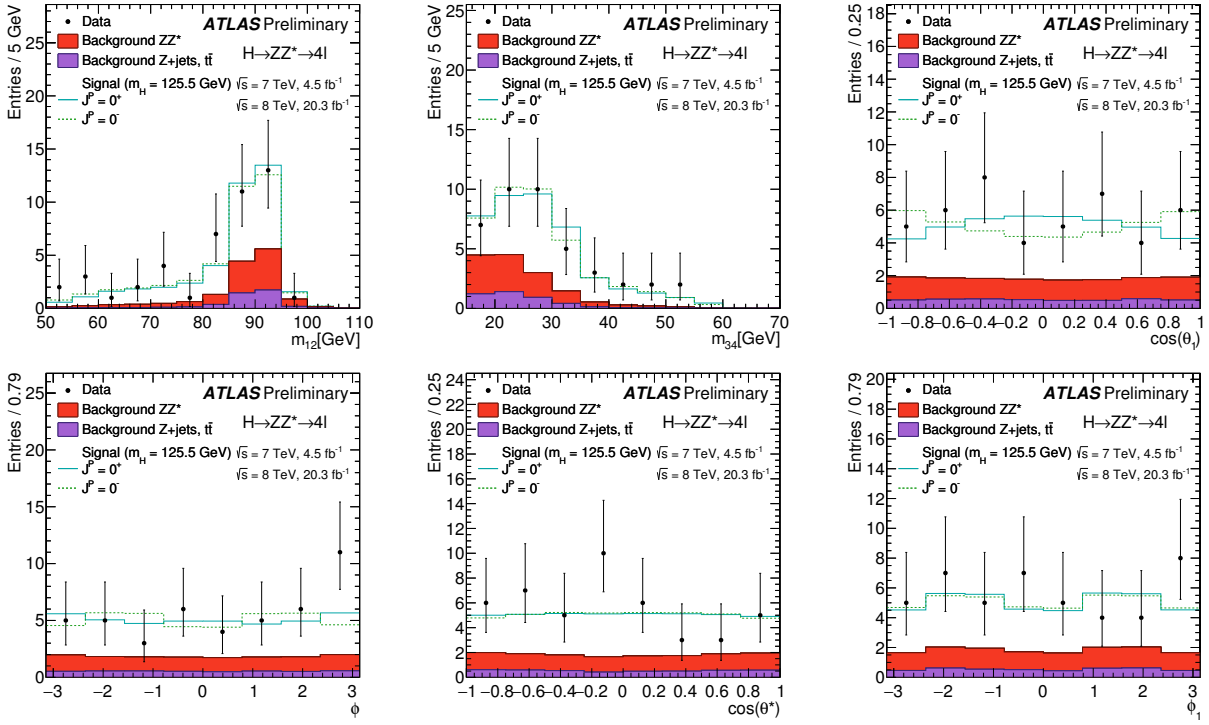

Figure 4: Distributions of the final state observables sensitive to the spin and parity of decaying resonance in the $H \to ZZ^* \to 4\ell$ signal region 115 GeV $< m_{4\ell} <$ 130 GeV for the data (point with errors), the backgrounds (filled histograms) and several spin hypotheses (SM solid line and alternatives dashed lines). Top row, left to right: invariant masses m_{12} , m_{34} and angle $\cos\theta_1$. Bottom row, left to right:, angles Φ, $\cos\theta^*$ and Φ_1.

uncertainty on the estimate of the fraction of 4μ and $4e$ candidates with an incorrect pairing of leptons is also considered. This uncertainty was derived by comparing the corresponding prediction obtained from the Powheg and JHU Monte Carlo generators for the Standard Model hypothesis. A conservative variation of ±10% to the incorrect pairing fraction was applied to all spin and parity hypotheses.

Source of the systematic uncertainty	J^P – MELA
Higgs boson mass modelling	±2%
ZZ^* pdf	±0.8%
Muons momentum scale	±0.7%
$Zbb \to ll\mu\mu$ normalisation	±0.6%
ZZ^* scale	±0.6%
Luminosity	±0.6%
e/γ resolution model (Sampling Term)	±0.5%
e/γ resolution model (Constant Term)	±0.5%
$Z \to llee$ normalisation	±0.5%
Fraction of wrongly paired 4ℓ candidates	±0.4%

Table 5: Relative impact of the main systematic uncertainties on $J^P = 0^+$ and $J^P = 0^-$ hypotheses separation for the J^P – MELA analysis.

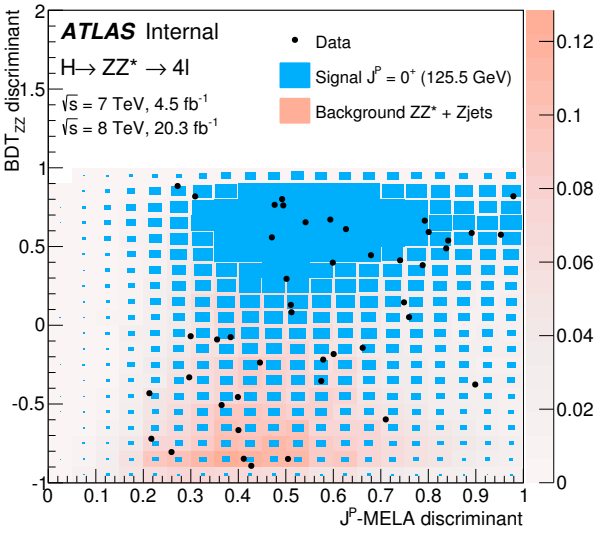

Figure 5: The distributions of the background discriminant BDT_{ZZ} versus the J^P – MELA discriminant for the $J^P = 0^+$ and $J^P = 0^-$ signal hypotheses in the signal region 115 GeV $< m_{4\ell} <$ 130 GeV.

The influence of the main systematic uncertainties on the $J^P = 0^+$ and $J^P = 0^-$ hypotheses separation for J^P – MELA analysis is presented in Table 5. The total impact of all systematic uncertainties on the final result is estimated to be about ±3%.

5.5 Individual and combined results

In this section the results from the analyses described above are presented, together with their combination. The distributions of discriminant variables in the data are in agreement with SM predictions and exclusions on the alternative spin hypothesis are derived. The results obtained from the fit to the data, expressed in terms of p-values for different tested hypotheses and observed $\mathrm{CL_s}$ for the alternative hypotheses, are summarised for all tested models in Tables 6 and 7.

Some examples of distributions of the test statistic q (defined in section 5.1) used to derive the results are presented in Figure 6. In these Figures, the observed value is indicated by the vertical solid line and the expected medians by the dashed lines. The signal strengths per decay channel and per centre-of-mass energy are treated as independent parameters during each fit. Their values are compatible with the SM predictions.

6 Study of the HVV interaction tensor structure

Following the discussion in Section 3, measurements of the HVV interaction tensor couplings κ_{SM}, κ_{AVV}, κ_{HVV} and of the mixing angle α are performed. The measurements consist of fitting the ratios of couplings $(\tilde{\kappa}_{AVV}/\kappa_{\mathrm{SM}}) \cdot \tan\alpha$ and $\tilde{\kappa}_{HVV}/\kappa_{\mathrm{SM}}$ to the discriminant observables for $H \to WW^* \to e\nu\mu\nu$ and $H \to ZZ^* \to 4\ell$ processes and in their combination. In the fitting procedure only one ratio of couplings is considered at a time, while the other BSM contribution is assumed to be absent.

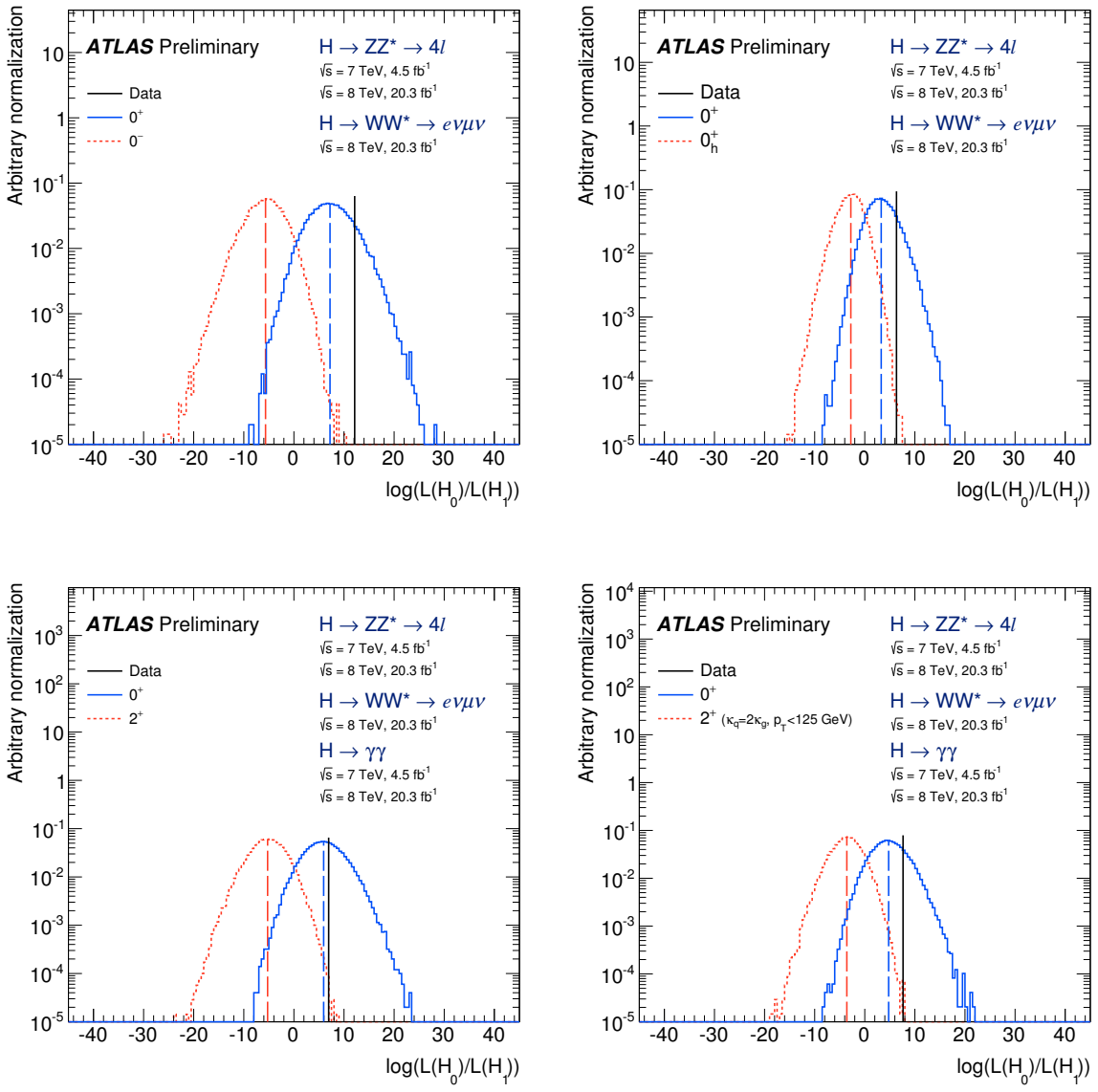

Figure 6: Examples of distributions of the test statistic q defined in section 5, for the combination of decay channels. **Top row:** combination of results obtained in $H \to ZZ^* \to 4\ell$ and $H \to WW^* \to e\nu\mu\nu$ analyses for the spin-0 hypothesis. Left: pseudo-scalar hypothesis. Right: BSM scalar hypothesis. **Bottow row:** combination of results obtained in $H \to ZZ^* \to 4\ell$ and $H \to WW^* \to e\nu\mu\nu$ and $H \to \gamma\gamma$ analyses for the spin-2 hypothesis. Left: spin-2 model with Universal couplings. Right: spin-2 model with with low gluon fraction and p_T cut-off at 125 GeV.

Tested Hypothesis	$H \to \gamma\gamma$				
	$p^{ALT}_{exp,\mu=1}$	$p^{ALT}_{exp,\mu=\hat{\mu}}$	p^{SM}_{obs}	p^{ALT}_{obs}	Obs. CL_s (%)
2^+	0.13	$7.5 \cdot 10^{-2}$	0.13	0.34	39
$2^+(\kappa_q = 0;\ p_T < 300)$	$4.3 \cdot 10^{-4}$	$< 3.1 \cdot 10^{-5}$	0.16	$2.9 \cdot 10^{-4}$	$3.5 \cdot 10^{-2}$
$2^+(\kappa_q = 0;\ p_T < 125)$	$9.4 \cdot 10^{-2}$	$5.6 \cdot 10^{-2}$	0.23	0.20	26
$2^+(\kappa_q = 2\kappa_g;\ p_T < 300)$	$9.1 \cdot 10^{-4}$	$< 3.1 \cdot 10^{-5}$	0.16	$8.6 \cdot 10^{-4}$	0.10
$2^+(\kappa_q = 2\kappa_g;\ p_T < 125)$	0.27	0.24	0.20	0.54	68
Tested Hypothesis	$H \to WW^* \to e\nu\mu\nu$				
	$p^{ALT}_{exp,\mu=1}$	$p^{ALT}_{exp,\mu=\hat{\mu}}$	p^{SM}_{obs}	p^{ALT}_{obs}	Obs. CL_s (%)
0^+_h	0.31	0.29	0.91	$2.7 \cdot 10^{-2}$	29
0^-	$6.4 \cdot 10^{-2}$	$3.2 \cdot 10^{-2}$	0.65	$1.2 \cdot 10^{-2}$	3.5
2^+	$6.4 \cdot 10^{-2}$	$3.3 \cdot 10^{-2}$	0.25	0.12	16
$2^+(\kappa_q = 0;\ p_T < 300)$	$1.5 \cdot 10^{-2}$	$4.0 \cdot 10^{-3}$	0.55	$3.0 \cdot 10^{-3}$	0.6
$2^+(\kappa_q = 0;\ p_T < 125)$	$5.6 \cdot 10^{-2}$	$2.9 \cdot 10^{-2}$	0.42	$4.4 \cdot 10^{-2}$	7.5
$2^+(\kappa_q = 2\kappa_g;\ p_T < 300)$	$1.5 \cdot 10^{-2}$	$4.0 \cdot 10^{-3}$	0.52	$3.0 \cdot 10^{-3}$	0.7
$2^+(\kappa_q = 2\kappa_g;\ p_T < 125)$	$4.4 \cdot 10^{-2}$	$2.2 \cdot 10^{-2}$	0.69	$7.0 \cdot 10^{-3}$	2.2
Tested Hypothesis	$H \to ZZ^* \to 4\ell$				
	$p^{ALT}_{exp,\mu=1}$	$p^{ALT}_{exp,\mu=\hat{\mu}}$	p^{SM}_{obs}	p^{ALT}_{obs}	Obs. CL_s (%)
0^+_h	$3.2 \cdot 10^{-2}$	$5.2 \cdot 10^{-3}$	0.80	$3.6 \cdot 10^{-4}$	0.18
0^-	$8.0 \cdot 10^{-3}$	$3.6 \cdot 10^{-4}$	0.88	$1.2 \cdot 10^{-5}$	$1.0 \cdot 10^{-2}$
2^+	$3.3 \cdot 10^{-2}$	$5.7 \cdot 10^{-4}$	0.91	$3.6 \cdot 10^{-5}$	$4.0 \cdot 10^{-2}$
$2^+(\kappa_q = 0;\ p_T < 300)$	$3.9 \cdot 10^{-2}$	$9.0 \cdot 10^{-3}$	0.95	$2.7 \cdot 10^{-5}$	$5.4 \cdot 10^{-2}$
$2^+(\kappa_q = 0;\ p_T < 125)$	$4.6 \cdot 10^{-2}$	$1.1 \cdot 10^{-2}$	0.93	$3.0 \cdot 10^{-5}$	$4.3 \cdot 10^{-2}$
$2^+(\kappa_q = 2\kappa_g;\ p_T < 300)$	$4.6 \cdot 10^{-2}$	$1.1 \cdot 10^{-2}$	0.66	$3.3 \cdot 10^{-3}$	0.97
$2^+(\kappa_q = 2\kappa_g;\ p_T < 125)$	$5.0 \cdot 10^{-2}$	$1.3 \cdot 10^{-2}$	0.88	$3.2 \cdot 10^{-4}$	0.27

Table 6: Expected and observed p-values for different spin-parity hypotheses, for each of the three analyses $H \to \gamma\gamma$, $H \to ZZ^* \to 4\ell$, and $H \to WW^* \to e\nu\mu\nu$. The observed CL_s for the alternative hypothesis is reported in the last column. The expected and observed p-values and the observed CL_s are defined in Section 5.5 and the alternative hypotheses are those described in Section 3.

6.1 Statistical treatment

The measurement of the tensor structure of the HVV interaction is based on a profile likelihood [29] that contains the discriminant observables sensitive to the EFT couplings. The signal rates in the different channels and for different centre-of-mass energies are treated as independent parameters. Therefore, the global signal normalisation is not used to constrain the EFT couplings. The ratios of the BSM to SM couplings, $\tilde{\kappa}_{HVV}/\kappa_{SM}$ and $(\tilde{\kappa}_{AVV}/\kappa_{SM}) \cdot \tan\alpha$, are each separately fit to the discriminant observables in data. The test statistic is $q' = -2\ln(\lambda)$, i.e. minus twice the logarithm of the profiled likelihood [29]. This test statistic is used to derive the confidence intervals on the parameters of interest. The results presented in the following rely on the asymptotic approximation [29] for the test statistic. This approximation was cross-checked with Monte Carlo ensemble tests that confirm its validity in the range of the parameters for which the 95% confidence level (CL) limits are derived.

Tested Hypothesis	$p^{ALT}_{exp,\mu=1}$	$p^{ALT}_{exp,\mu=\hat{\mu}}$	p^{SM}_{obs}	p^{ALT}_{obs}	Obs. CL_S (%)
0^+_h	$2.5 \cdot 10^{-2}$	$4.7 \cdot 10^{-3}$	0.85	$7.1 \cdot 10^{-5}$	$4.7 \cdot 10^{-2}$
0^-	$1.8 \cdot 10^{-3}$	$1.3 \cdot 10^{-4}$	0.88	$< 3.1 \cdot 10^{-5}$	$< 2.6 \cdot 10^{-2}$
2^+	$4.3 \cdot 10^{-3}$	$2.9 \cdot 10^{-4}$	0.61	$4.3 \cdot 10^{-5}$	$1.1 \cdot 10^{-2}$
$2^+(\kappa_q = 0;\ p_T < 300)$	$< 3.1 \cdot 10^{-5}$	$< 3.1 \cdot 10^{-5}$	0.52	$< 3.1 \cdot 10^{-5}$	$< 6.5 \cdot 10^{-3}$
$2^+(\kappa_q = 0;\ p_T < 125)$	$3.4 \cdot 10^{-3}$	$3.9 \cdot 10^{-4}$	0.71	$4.3 \cdot 10^{-5}$	$1.5 \cdot 10^{-2}$
$2^+(\kappa_q = 2\kappa_g;\ p_T < 300)$	$< 3.1 \cdot 10^{-5}$	$< 3.1 \cdot 10^{-5}$	0.28	$< 3.1 \cdot 10^{-5}$	$< 4.3 \cdot 10^{-3}$
$2^+(\kappa_q = 2\kappa_g;\ p_T < 125)$	$7.8 \cdot 10^{-3}$	$1.2 \cdot 10^{-3}$	0.80	$7.3 \cdot 10^{-5}$	$3.7 \cdot 10^{-2}$

Table 7: Expected and observed p-values for different spin-parity hypotheses, for the combination of the three channels: $H \to \gamma\gamma$, $H \to ZZ^* \to 4\ell$ and $H \to WW^* \to e\nu\mu\nu$. The observed CL_s for the alternative hypothesis is reported in the last column. The expected and observed p-values and the observed CL_S are defined in Section 5.5. The definitions of alternative hypotheses are given in Section 3.

6.2 Tensor structure analyses in the $H \to WW^* \to e\nu\mu\nu$ channel

The $H \to WW^* \to e\nu\mu\nu$ analysis used to study the spin-0 tensor structure is already described in Section 5.3 and detailed in Ref. [8]. Only the 0-jet category is considered and the BDT_0 and BDT_{CP} are used as discriminant variables in the likelihood defined to measure the spin-0 tensor structure couplings. The only difference with respect to the spin hypothesis test is that, in this analysis, the BSM spin-0 couplings are treated as continuous variables in the test statistic.

6.3 Tensor structure analyses in the $H \to ZZ^* \to 4\ell$ channel

To allow for a cross-check and validation of the obtained results, two different fitting methods based on the analytical calculation of the leading order matrix element of the $H \to ZZ^* \to 4\ell$ process are used.

The method of the matrix element observable fit is based on modelling the distributions of the final state observables in each bin of coupling ratios using Monte Carlo. Using the Lagrangian defined in Eq. 1 which is linear in the coupling constants κ_{SM}, κ_{HVV} and κ_{AVV}, the differential cross section at each point in the phase-space can be expressed as a term corresponding to the SM amplitude, plus two additional terms, linear and quadratic in the coupling constants. In this way it is possible to define two observables for each coupling, the so-called first and second order optimal observables, upon which the amplitude depends at each point of the phase-space. For each event, they contain the full kinematic information about the couplings, that can thus be extracted from a fit to their shapes. More details on the method can be found in Refs. [38, 39].

The observables sensitive to the presence and structure of κ_{SM}, κ_{HVV} and κ_{AVV} considered in the current analysis are defined as follows:

$$
\begin{aligned}
O_1(\kappa_{HVV}) &= \frac{2\Re(ME(\kappa_{SM}\neq 0;\,\kappa_{HVV},\kappa_{AVV}=0;\,\alpha=0)^* \cdot ME(\kappa_{HVV}\neq 0;\,\kappa_{SM},\kappa_{AVV}=0;\,\alpha=0))}{|ME(\kappa_{SM}\neq 0;\,\kappa_{HVV},\kappa_{AVV}=0;\,\alpha=0)|^2}, \\
O_2(\kappa_{HVV}) &= \frac{|ME(\kappa_{HVV}\neq 0;\,\kappa_{SM},\kappa_{AVV}=0;\,\alpha=0)|^2}{|ME(\kappa_{SM}\neq 0;\,\kappa_{HVV},\kappa_{AVV}=0;\,\alpha=0)|^2}, \\
O_1(\kappa_{AVV},\alpha) &= \frac{2\Re(ME(\kappa_{SM}\neq 0;\,\kappa_{HVV},\kappa_{AVV}=0;\,\alpha=0)^* \cdot ME(\kappa_{AVV}\neq 0;\,\kappa_{SM},\kappa_{HVV}=0;\,\alpha=\pi/2))}{|ME(\kappa_{SM}\neq 0;\,\kappa_{HVV},\kappa_{AVV}=0;\,\alpha=0)|^2}, \\
O_2(\kappa_{AVV},\alpha) &= \frac{|ME(\kappa_{AVV}\neq 0;\,\kappa_{SM},\kappa_{HVV}=0;\,\alpha=\pi/2)|^2}{|ME(\kappa_{SM}\neq 0;\,\kappa_{HVV},\kappa_{AVV}=0;\,\alpha=0)|^2}.
\end{aligned}
\tag{10}
$$

Here the $ME(\kappa_{\rm SM}, \kappa_{HVV}, \kappa_{AVV}, \alpha)$ denotes the leading order matrix element of the $H \to ZZ^* \to 4\ell$ process. These definitions correspond to the first- and second-order optimal observables for a BSM amplitude with a three-component structure.

The observables $O_{1,2}(\kappa_{HVV})$ and $O_{1,2}(\kappa_{AVV}, \alpha)$ are used for the $\tilde{\kappa}_{HVV}/\kappa_{\rm SM}$ and $(\tilde{\kappa}_{AVV}/\kappa_{\rm SM}) \cdot \tan\alpha$ individual fits respectively. In order to suppress the ZZ^* background, a kinematic BDT discriminant similar to those described in Section 5.4 is used as an additional observable in all fits. The BDT training is performed independently for each final state using parity-independent observables: η_{4l}, p_T^{4l}, m_{4l}, $\cos(\theta^*)$ and ϕ_1. This BDT discriminant will be denoted hereafter as the BDT(ZZ).

The distributions of observables defined in Eq. 10 for the Monte Carlo signal samples generated with $(\tilde{\kappa}_{HVV}/\kappa_{\rm SM} = 0, \pm 1; \kappa_{AVV} = 0)$ and $((\tilde{\kappa}_{AVV}/\kappa_{\rm SM}) \cdot \tan\alpha = 0, \pm 5; \kappa_{HVV} = 0)$ are shown in Figure 7. The contributions of all backgrounds considered in this analysis are also included. By construction the O_2 observables are sensitive to the modulus of the $\tilde{\kappa}_{HVV}/\kappa_{\rm SM}$ and $\tilde{\kappa}_{AVV}/\kappa_{\rm SM} \tan\alpha$ ratios: their distributions change with the strength of the respective coupling constants. These observables are insensitive to the relative sign of κ_{HVV} and κ_{AVV} with respect to $\kappa_{\rm SM}$. The sign sensitivity comes from the O_1 observables which are based on the interference terms: their distributions feature pronounced sign-dependent asymmetries.

The analysis is performed in several steps. First, multidimensional histograms of observables are created in 22 bins of $\tilde{\kappa}_{HVV}/\kappa_{\rm SM}$ and $\tilde{\kappa}_{AVV}/\kappa_{\rm SM} \cdot \tan\alpha$ for all fits. The predicted shapes of the observables for the signal are produced by re-weighting the base Monte Carlo sample described in Section 4. The corresponding weights are derived using the analytical calculation of the $H \to ZZ^* \to 4\ell$ matrix elements at leading order. The weights are calculated and applied at the Monte Carlo generator level. The observables used in the analysis are evaluated after detector simulation, accounting for the detector acceptance, resolution and reconstruction efficiency. The distributions of observables for backgrounds are estimated using the Monte Carlo (for the irreducible background) and data-driven techniques (for the reducible backgrounds) described in Section 5 and Ref. [35].

In the fits of $\tilde{\kappa}_{HVV}/\kappa_{\rm SM}$ and $(\tilde{\kappa}_{AVV}/\kappa_{\rm SM}) \cdot \tan\alpha$ only one BSM contribution is considered at a time and the distributions of observables are three-dimensional: O_1, O_2 and BDT(ZZ). To obtain a reliable description for bins with insufficient number of Monte Carlo events, the Kernel Density Estimation smoothing procedure is applied to signal and background multidimensional histograms. In the smoothing procedure the smearing is done separately in four bins of BDT(ZZ), preserving the original normalisation.

The final PDFs used in the fits are obtained by applying linear histogram interpolation between the multidimensional bins of $\tilde{\kappa}_{HVV}/\kappa_{\rm SM}$ and $(\tilde{\kappa}_{AVV}/\kappa_{\rm SM}) \cdot \tan\alpha$. The individual likelihood functions per collision energy ($\sqrt{s}$) and final state (FS) are:

$$\mathcal{L}\left(\bar{\Omega}\middle|\frac{\tilde{\kappa}_{HVV}}{\kappa_{\rm SM}}, \frac{\tilde{\kappa}_{AVV}}{\kappa_{\rm SM}}\tan\alpha, \theta\right) = \prod_i P\left[\bar{\Omega}_i\middle|s_i\left(\frac{\tilde{\kappa}_{HVV}}{\kappa_{\rm SM}}, \frac{\tilde{\kappa}_{AVV}}{\kappa_{\rm SM}}\tan\alpha, \theta\right) + b_i(\theta)\right], \tag{11}$$

where P is the probability density function for the data vector $\bar{\Omega}$, given the signal model s and background model b. The index i runs over all the bins of multidimensional histograms of observables and θ represents the vector of nuisance parameters corresponding to systematic uncertainties. Fits to data are performed by minimising the negative likelihood function with respect to ratios of couplings:

$$L\left(\bar{\Omega}\middle|\frac{\tilde{\kappa}_{HVV}}{\kappa_{\rm SM}}, \frac{\tilde{\kappa}_{AVV}}{\kappa_{\rm SM}}\tan\alpha, \theta\right) = -2\ln\prod_{\sqrt{s}}\prod_{\rm FS}\mathcal{L}\left(\bar{\Omega}\middle|\frac{\tilde{\kappa}_{HVV}}{\kappa_{\rm SM}}, \frac{\tilde{\kappa}_{AVV}}{\kappa_{\rm SM}}\tan\alpha, \theta\right). \tag{12}$$

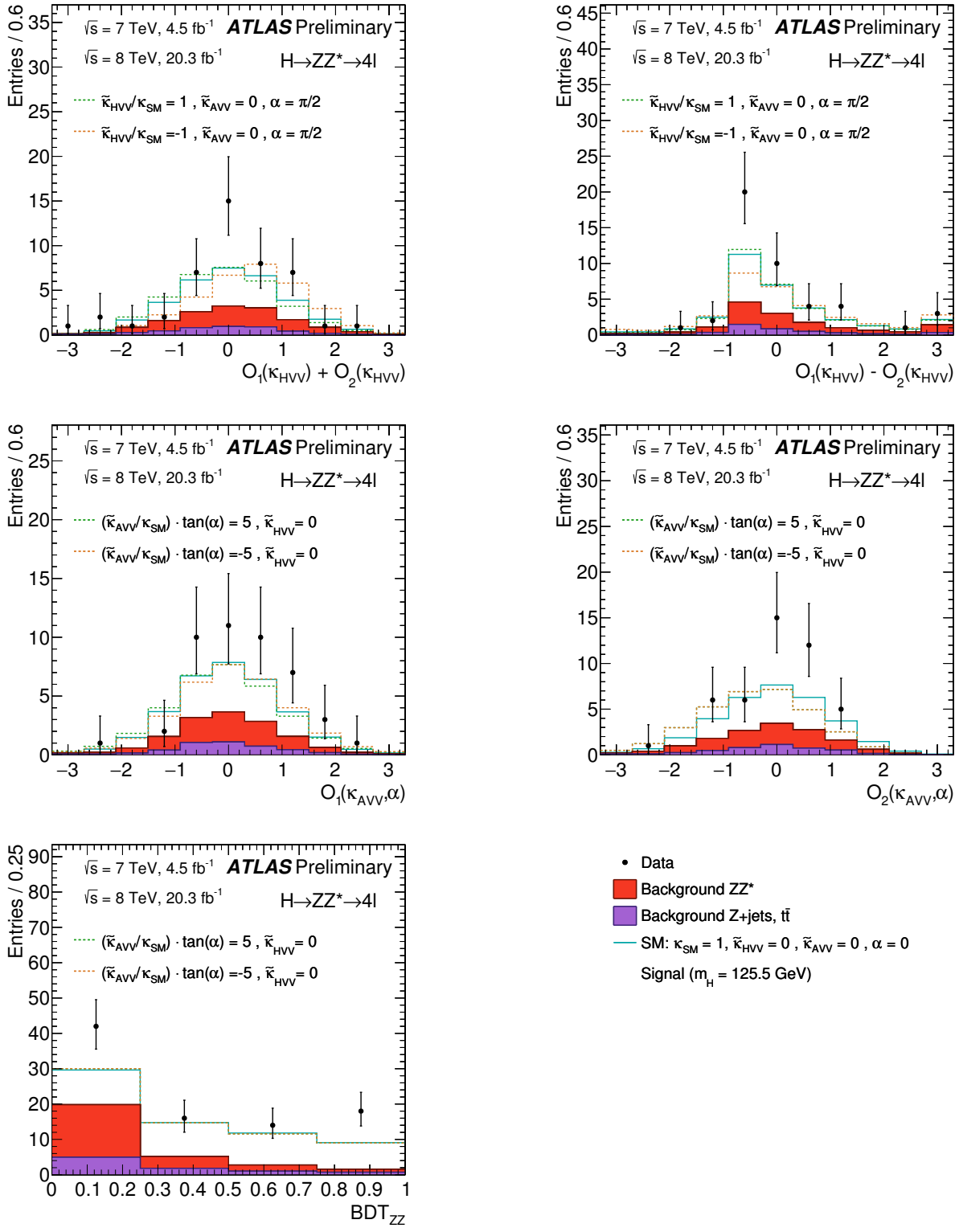

Figure 7: Examples of distributions of observables used in the matrix element observable fit. Top row left: $O_1(\tilde{\kappa}_{HVV}) + O_2(\tilde{\kappa}_{HVV})$, right: $O_1(\tilde{\kappa}_{HVV}) - O_2(\tilde{\kappa}_{HVV})$, for the Monte Carlo signal generated with $(\tilde{\kappa}_{HVV}/\kappa_{\rm SM} = 0, \pm 1; \kappa_{AVV} = 0)$. Middle row left: $O_1(\tilde{\kappa}_{AVV} \cdot \alpha)$, right: $O_2(\tilde{\kappa}_{AVV} \cdot \alpha)$ for the Monte Carlo signal generated with $((\tilde{\kappa}_{AVV}/\kappa_{\rm SM}) \cdot \tan\alpha = 0, \pm 5; \kappa_{HVV} = 0)$. Bottom row left: BDT$(ZZ)$ for the Monte Carlo signal generated with $(\tilde{\kappa}_{HVV}/\kappa_{\rm SM} = 0, \pm 1; \kappa_{AVV} = 0)$. The expected background contributions are shown as filled histograms on each plot.

The test statistic q' is defined as the profiled value of L of Eq. 12. To ensure the correctness of the statistical treatment and the absence of significant biases, a series of tests were performed before applying the fit to the data. Asimov datasets [29] created from independently generated Monte Carlo samples with $\tilde{\kappa}_{HVV}/\kappa_{\rm SM}$ and $(\tilde{\kappa}_{AVV}/\kappa_{\rm SM}) \cdot \tan\alpha$ equal to $0, \pm 2, \pm 4, \pm 6, \pm 8$ and ± 10 were injected into the analysis procedure. The tests were repeated for samples corresponding to one and one hundred times LHC Run-I luminosity. In all cases the fitted values of coupling constants were found to be in agreement with the injected values within statistical uncertainties.

The results of the matrix element observable fit were validated and cross-checked using a nine-dimensional matrix element method (9D fit). The method implements a multivariate per-event extended likelihood that is sensitive to both the $\tilde{\kappa}_{HVV}/\kappa_{\rm SM}$ and $(\tilde{\kappa}_{AVV}/\kappa_{\rm SM}) \cdot \tan\alpha$ mixing parameters and is based on the nine experimental observable defined as follows. The probability model is constructed with separate components for signal, the SM ZZ^* background, and the reducible background. The background components are assumed to be independent of the Higgs boson tensor structure, so all of the sensitivity to mixing parameters comes from the signal component. Each component depends on nine experimental observables: $m_{4\ell}$, $p_{T,4\ell}$, $\eta_{4\ell}$, $\cos\theta^*$, $\cos\theta_1$, $\cos\theta_2$, Φ, m_{12} and m_{34} (described in Section 5.4). Of these observables, $\cos\theta_1$, $\cos\theta_2$, Φ, m_{12}, and m_{34} have distributions that depend on the coupling constants at parton-level. The others are included in the probability model in order to separate the signal from the backgrounds. The complete probability model is the same as in Eq. 11, with the only difference being the dimensionality of the observables vector Ω which in this case is a nine-dimensional vector. In the 9D fit, the observable-space is simplified by ignoring small correlations and thereby factoring the nine-dimensional distributions into multiple distributions each one depending on a subset of the nine observables. In this way, the MC can be used to construct the signal and background shapes for each distribution. For the signal component the leading order matrix element of the HZZ process $ME(\kappa_{\rm SM}, \kappa_{HVV}, \kappa_{AVV}, \alpha)$ is used in addition to MC to help retain more correlation information.

In this note, only results based on the matrix element observable approach are reported. The 9D approach was used as a cross-check and produced results compatible with the matrix element approach. Some of the results obtained with the 9D approach are shown in Appendix B.

The main sources of systematic uncertainties for the tensor structure measurements are the same as discussed in Section 5 since they are based on the same four-lepton variables. Several additional sources of uncertainty, specific to each of the methods, are also taken into account. For the matrix element observable fit, the uncertainty related to the Kernel Density Estimation smoothing procedure applied to signal and background multidimensional histograms is considered. To estimate the influence of this uncertainty on the final result, a procedure similar to the one described in Section 5 is employed. The impact of the different sources of systematic uncertainties on the final results is evaluated by comparing the BSM exclusion limits obtained with a specific systematic uncertainty included or excluded in the fit, while excluding all other systematic uncertainties. A similar conclusions holds to that in the fixed hypothesis test: the systematic uncertainties have a very limited impact on the final result. The most important uncertainties are related to the estimates of the reducible backgrounds. The relative impact of these uncertainties on the final 95% CL exclusion limit on BSM couplings was found to be around $\pm 1\%$. The second most important group of sources of systematic uncertainties is related to the theoretical uncertainties on the ZZ background production cross-sections. Their relative impact on the final result is found to be below $\pm 1\%$. The precision of the tensor structure analysis is thus dominated by the statistical errors.

6.4 Individual and combined results

The results of the tensor structure analyses performed in the $H \to WW^* \to e\nu\mu\nu$ channel are reported in Ref. [8] and, for completeness, they are also summmarised in Table 8.

Coupling ratio	Best fit value		95% CL Exclusion Regions	
$H \to WW^* \to e\nu\mu\nu$	Expected	Observed	Expected	Observed
$\tilde{\kappa}_{HVV}/\kappa_{\mathrm{SM}}$	0.0	-1.3	$[-1.2, -0.7]$	$(-\infty, -2.2] \bigcup [-1, -0.85] \bigcup [0.4, \infty)$
$(\tilde{\kappa}_{AVV}/\kappa_{\mathrm{SM}}) \cdot \tan\alpha$	0.0	-0.2	–	$(-\infty, -6] \bigcup [5, \infty)$

Table 8: Fitted values of $\tilde{\kappa}_{HVV}/\kappa_{\mathrm{SM}}$ and $(\tilde{\kappa}_{AVV}/\kappa_{\mathrm{SM}}) \cdot \tan\alpha$ and 95% CL excluded regions obtained in $H \to WW^* \to e\nu\mu\nu$ analysis. The expected values are produced for the signal strength measured in data and assuming best fit values for all other nuisance parameters. Only data collected at $\sqrt{s} = 8$ TeV are used. The symbol "–" denotes the absence of 95% CL sensitivity.

The distributions of the test statistic for fits of $\tilde{\kappa}_{HVV}/\kappa_{\mathrm{SM}}$ and $(\tilde{\kappa}_{AVV}/\kappa_{\mathrm{SM}}) \cdot \tan\alpha$ measured in the $H \to ZZ^* \to 4\ell$ analysis are shown in Figure 8. These results are obtained assuming only one BSM

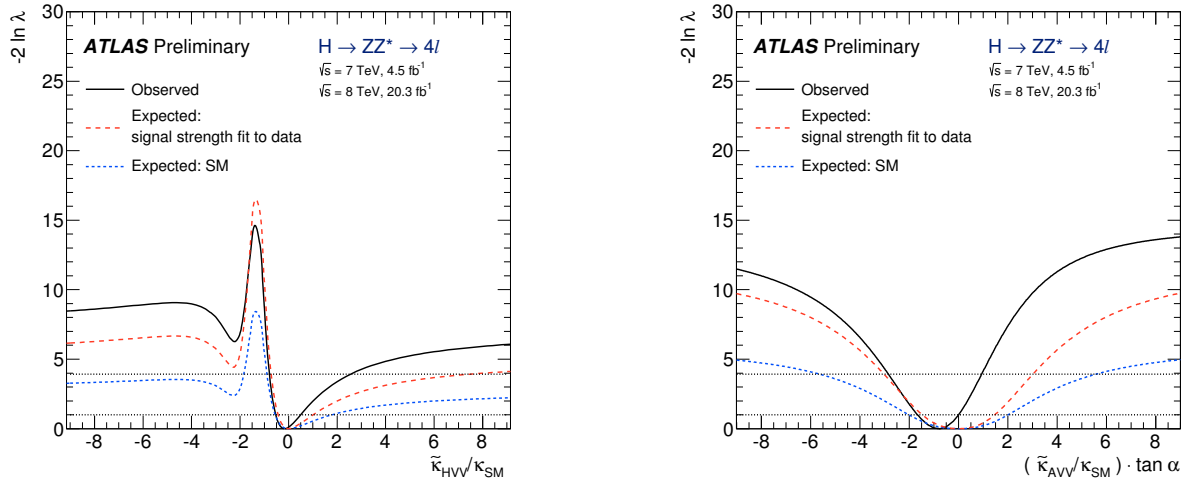

Figure 8: Expected and observed distributions of the test statistic for fits of $\tilde{\kappa}_{HVV}/\kappa_{\mathrm{SM}}$ (left) and $(\tilde{\kappa}_{AVV}/\kappa_{\mathrm{SM}}) \cdot \tan\alpha$ (right) for the $H \to ZZ^* \to 4\ell$ analysis. The expected curves are calculated assuming the Standard Model $J^P = 0^+$ signal and produced with the Standard Model signal strength $\mu = 1$ and with the signal strength fitted to data: $\hat{\mu}$. The horizontal dotted black lines represent the levels of $-2\ln\lambda$ above which the values of coupling ratios under study are excluded above 68 and 95% CL, respectively.

contribution to be present at a time. The expected curves are calculated assuming the Standard Model $J^P = 0^+$ signal, both with the Standard Model signal strength, $\mu = 1$, and with the signal strength fitted to data, $\hat{\mu}$. The fitted values of $\tilde{\kappa}_{HVV}/\kappa_{\mathrm{SM}}$ and $(\tilde{\kappa}_{AVV}/\kappa_{\mathrm{SM}}) \cdot \tan\alpha$, together with the intervals where these couplings are excluded above 95% CL, are reported in Table 9. The fitted values agree with the Standard Model predictions within the uncertainties.

The measurements from the $H \to WW^* \to e\nu\mu\nu$ and $H \to ZZ^* \to 4\ell$ channels are combined under the assumption that the BSM ratios of couplings $\tilde{\kappa}_{HVV}/\kappa_{\mathrm{SM}}$ and $(\tilde{\kappa}_{AVV}/\kappa_{\mathrm{SM}}) \cdot \tan\alpha$ are the same for the W and Z vector bosons. A common test statistic is obtained by combining the individual channels profiled

Coupling ratio	Best fit value		95% CL Exclusion Regions	
$H \to ZZ^* \to 4\ell$	Expected	Observed	Expected	Observed
$\tilde{\kappa}_{HVV}/\kappa_{\rm SM}$	0.0	−0.2	$(-\infty, -0.75] \bigcup [6.95, \infty)$	$(-\infty, -0.75] \bigcup [2.45, \infty)$
$(\tilde{\kappa}_{AVV}/\kappa_{\rm SM}) \cdot \tan\alpha$	0.0	−0.8	$(-\infty, -2.95] \bigcup [2.95, \infty)$	$(-\infty, -2.85] \bigcup [0.95, \infty)$

Table 9: Expected and observed best fit values of $\tilde{\kappa}_{HVV}/\kappa_{\rm SM}$ and $(\tilde{\kappa}_{AVV}/\kappa_{\rm SM}) \cdot \tan\alpha$ and 95% CL excluded regions obtained in the $H \to ZZ^* \to 4\ell$ analysis. The expected values are produced for the signal strength measured in data and assuming best fit values for all other nuisance parameters. The data for $\sqrt{s} = 7$ TeV and $\sqrt{s} = 8$ TeV are combined.

likelihoods. The expected distributions of likelihoods for the the signal strength obtained from fit to data $\hat{\mu}$ are presented in the Figure 9. The observed distributions of profile likelihoods for the combination of

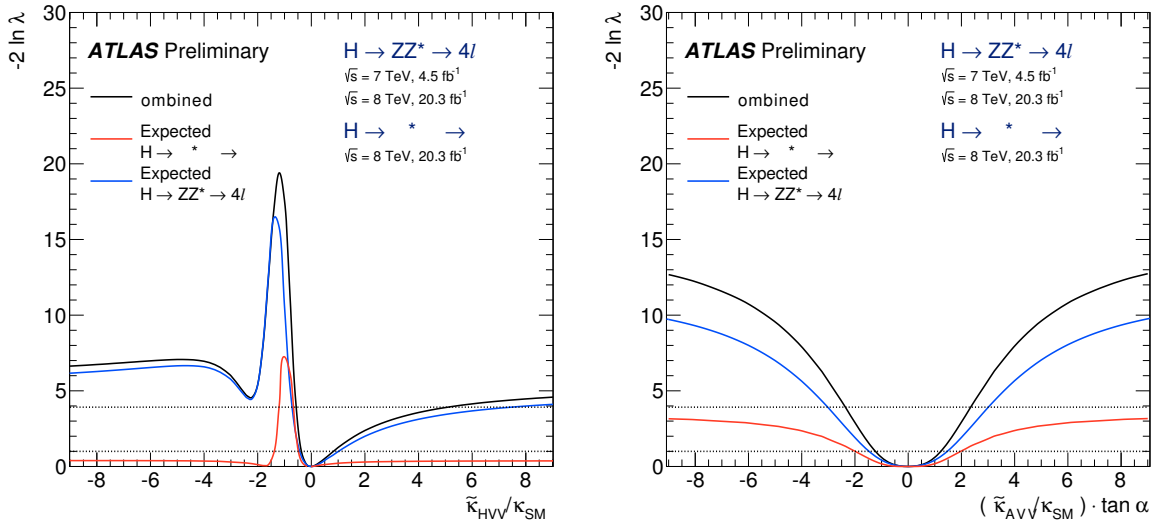

Figure 9: Expected distributions of of the test statistic for the combination of $H \to WW^* \to e\nu\mu\nu$ and $H \to ZZ^* \to 4\ell$ analyses. as a function of BSM coupling ratios $\tilde{\kappa}_{HVV}/\kappa_{\rm SM}$ and $(\tilde{\kappa}_{AVV}/\kappa_{\rm SM}) \cdot \tan\alpha$. The 68% and 95% CL exclusion regions are indicated as lying above the corresponding horizontal lines. The individual distributions for $H \to WW^* \to e\nu\mu\nu$ and $H \to ZZ^* \to 4\ell$ channels are shown.

$H \to WW^* \to e\nu\mu\nu$ and $H \to ZZ^* \to 4\ell$ measurements are presented in Figure 10. Here the signal rate normalisations are treated as independent nuisance parameters between the different decay channels and the different centre-of-mass energies. The other nuisance parameters related to the experimental and theoretical uncertainties are treated as correlated when appropriate. The resulting 95% CL exclusion regions for the combinations of $H \to WW^* \to e\nu\mu\nu$ and $H \to ZZ^* \to 4\ell$ channels are listed in the Table. 10.

7 Conclusion

Studies of the spin and parity of the recently observed Higgs boson in the $H \to ZZ^* \to 4\ell$, $H \to WW^* \to e\nu\mu\nu$ and $H \to \gamma\gamma$ decay processes at the LHC are presented. The investigations are based on 4.5 fb^{-1}

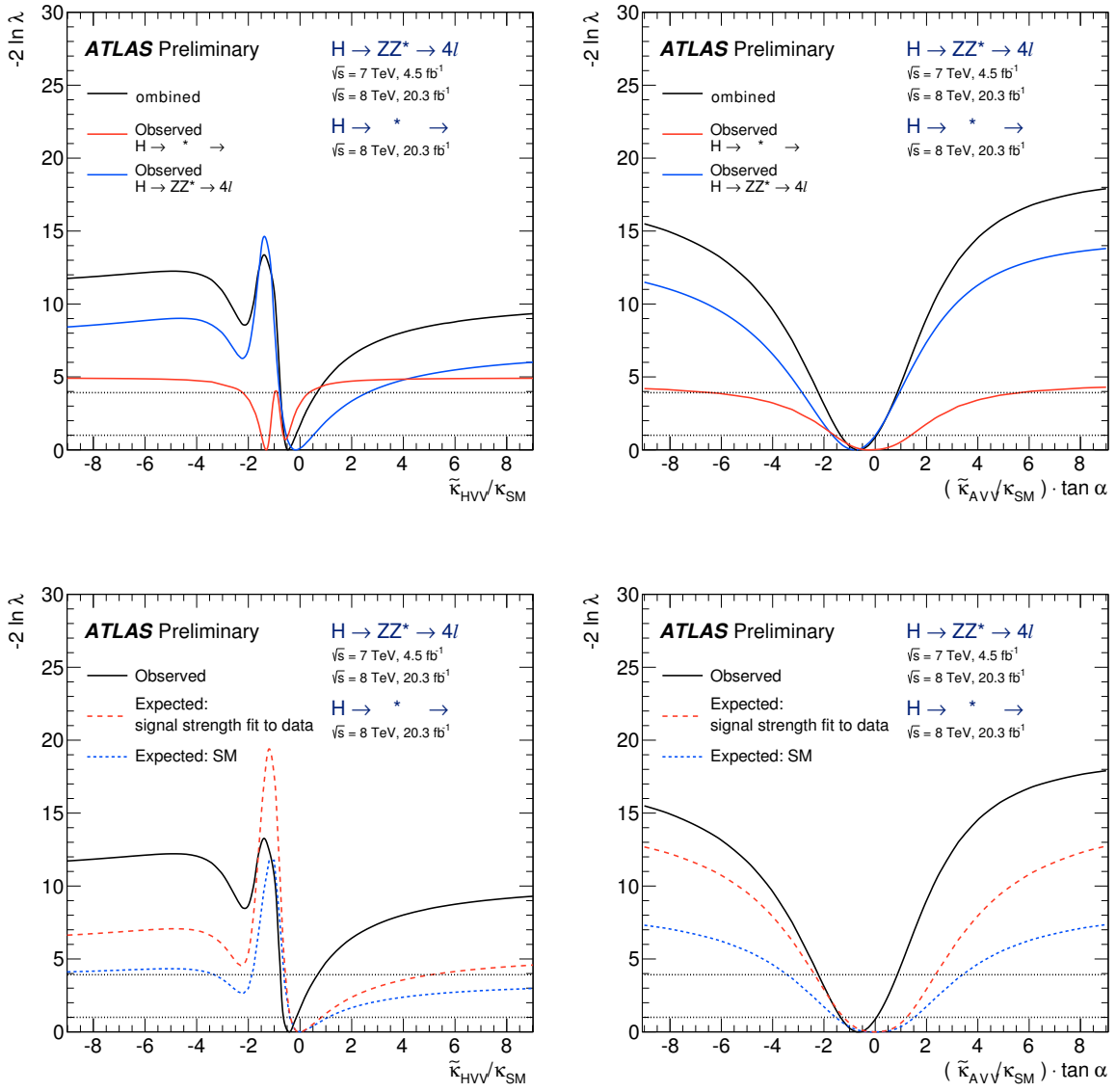

Figure 10: Observed and expected distributions the test statistic for $H \to WW^* \to e\nu\mu\nu$ and $H \to ZZ^* \to 4\ell$ analyses and their combinations. The distributions are shown as a function of BSM coupling ratios $\tilde{\kappa}_{HVV}/\kappa_{\rm SM}$ and $(\tilde{\kappa}_{AVV}/\kappa_{\rm SM}) \cdot \tan\alpha$, The 68% and 95% CL exclusion regions are indicated as lying above the corresponding horizontal lines. **Top row:** individual $H \to WW^* \to e\nu\mu\nu$, $H \to ZZ^* \to 4\ell$ and combined observed distributions. **Bottom row:** expected and observed combined distributions. The expected distributions are presented for the SM signal strength and for the signal strength obtained from the fit to data.

Coupling ratio	Best fit value		95% CL Exclusion Regions	
Combined	Expected	Observed	Expected	Observed
$\tilde{\kappa}_{HVV}/\kappa_{\mathrm{SM}}$	0.0	−0.48	$(-\infty, -0.55] \bigcup [4.80, \infty)$	$(-\infty, -0.73] \bigcup [0.63, \infty)$
$(\tilde{\kappa}_{AVV}/\kappa_{\mathrm{SM}}) \cdot \tan\alpha$	0.0	−0.68	$(-\infty, -2.33] \bigcup [2.30, \infty)$	$(-\infty, -2.18] \bigcup [0.83, \infty)$

Table 10: Expected and observed best fit values of $\tilde{\kappa}_{HVV}/\kappa_{\mathrm{SM}}$ and $(\tilde{\kappa}_{AVV}/\kappa_{\mathrm{SM}}) \cdot \tan\alpha$ and 95% CL excluded regions obtained in the combination of $H \to ZZ^* \to 4\ell$ and $H \to WW^* \to e\nu\mu\nu$ analyses. The expected values are produced for the signal strength measured in data and assuming best fit values for all other nuisance parameters. The signal strengths are treated independently per decay channel and per collision energy.

and 20.3 fb^{-1} of pp collision data collected by the ATLAS experiment at $\sqrt{s}$ = 7 TeV and $\sqrt{s}$ = 8 TeV respectively. The SM Higgs boson hypothesis, corresponding to the quantum numbers $J^P = 0^+$, is tested against several alternative spin models. They include a non-SM spin-0 and the spin-2 model with universal and non-universal couplings to fermions and vector bosons. The combination of the three decay processes allow the exclusion of all considered non-SM spin models at more then 99% CL in favour of the SM spin-0 hypothesis.

The tensor structure of the HVV interaction in the spin-0 hypothesis is also investigated using the $H \to ZZ^* \to 4\ell$ and $H \to WW^* \to e\nu\mu\nu$ decays. Only one BSM tensor coupling is investigated at a time, while the other one is set to zero. The observed distributions of the variables sensitive the ratios of the BSM to SM tensor couplings, $\tilde{\kappa}_{HVV}/\kappa_{\mathrm{SM}}$ and $(\tilde{\kappa}_{AVV}/\kappa_{\mathrm{SM}}) \cdot \tan\alpha$, are compatible with the predicted SM values. Values of the BSM tensor couplings outside of the regions $-0.75 < \tilde{\kappa}_{HVV}/\kappa_{\mathrm{SM}} < 2.45$ and $-2.85 < (\tilde{\kappa}_{AVV}/\kappa_{\mathrm{SM}}) \cdot \tan\alpha < 0.95$ are excluded at 95% CL for the $H \to ZZ^* \to 4\ell$ process. For the $H \to WW^* \to e\nu\mu\nu$ process the ranges $-2.2 < \tilde{\kappa}_{HVV}/\kappa_{\mathrm{SM}} < -1.0$ and $-0.85 < \tilde{\kappa}_{HVV}/\kappa_{\mathrm{SM}} < 0.4$ and $-6.0 < (\tilde{\kappa}_{AVV}/\kappa_{\mathrm{SM}}) \cdot \tan\alpha < 5.0$ are excluded at 95% CL. Under the assumption that the $\tilde{\kappa}_{HVV}/\kappa_{\mathrm{SM}}$ and $(\tilde{\kappa}_{AVV}/\kappa_{\mathrm{SM}}) \cdot \tan\alpha$ couplings have the same values for the HWW and HZZ processes, the results from the two decay channels are combined. As a result of this combination values of the BSM tensor couplings, the regions outside of $-0.73 < \tilde{\kappa}_{HVV}/\kappa_{\mathrm{SM}} < 0.63$ and $-2.18 < (\tilde{\kappa}_{AVV}/\kappa_{\mathrm{SM}}) \cdot \tan\alpha < 0.83$ are excluded at 95% CL. The corresponding expected not excluded regions at 95% CL, assuming the SM Higgs boson hypothesis, are $-0.55 < \tilde{\kappa}_{HVV}/\kappa_{\mathrm{SM}} < 4.80$ and $-2.33 < (\tilde{\kappa}_{AVV}/\kappa_{\mathrm{SM}}) \cdot \tan\alpha < 2.30$.

Appendix A

To compare the exclusion limits obtained in this analysis to other existing studies, the final results of this analysis are also expressed in terms of effective cross-section fractions (f_{g2}, ϕ_{g2}) and (f_{g4}, ϕ_{g4}). The definition proposed in Sec. 11.4.2 of Ref. [6] are used:

$$f_{gi} = \frac{|g_i|^2\sigma_i}{|g_1|^2\sigma_1 + |g_2|^2\sigma_2 + |g_4|^2\sigma_4}, \ \phi_i = \arg\left(\frac{g_i}{g_1}\right). \tag{13}$$

Here the symbols g_1, g_2 and g_4 denote the Standard Model, BSM CP-even and BSM CP-odd tensor couplings of the HVV scattering amplitude respectively. The numeric coefficients σ_1, σ_2 and σ_4 are effective cross sections of the HVV interactions calculated when only g_1, g_2 or g_4-related terms are present in amplitude, respectively, such that $g_i = 1, g_{i\neq j} = 0$.

In the case when in addition to the Standard Model term only one CP-even or CP-odd BSM contribution is present, the conversion between the parametrisation used in this analysis and the (f_{gi}, ϕ_{gi}) parametrisation is given by the Eq. 13 re-written in the following way:

$$f_{g_i} = \frac{r_{i1}^2}{1 + r_{i1}^2}; \quad (i = 2, 4), \tag{14}$$

where r_{41} and r_{21} are chosen such that:

$$r_{21}^2 = \frac{\sigma_{HVV}}{\sigma_{\rm SM}}\left(\frac{\tilde{k}_{HVV}}{k_{\rm SM}}\right)^2, \ \text{and} \ r_{41}^2 = \frac{\sigma_{AVV}}{\sigma_{\rm SM}}\left(\frac{\tilde{k}_{AVV}}{k_{\rm SM}}\right)^2 \tan^2\alpha. \tag{15}$$

The numeric coefficients $\sigma_{\rm SM}$, σ_{HVV} and σ_{AVV} are effective cross sections of the HVV interaction calculated when only $k_{\rm SM}$, k_{HVV} and k_{AVV}-related terms are present in the Lagrangian respectively.

For consistency with previous measurements reported in Ref. [4], the expected and observed results of the current analysis for $H \to WW^* \to e\nu\mu\nu$ and $H \to ZZ^* \to 4\ell$ channels and for their combination are expressed in terms of f_{gi} and ϕ_{gi} parameters for the $H \to ZZ^* \to 4\ell$ decay, $(f_{g2}^{ZZ}, \phi_{g2}^{ZZ})$ and $(f_{g4}^{ZZ}, \phi_{g4}^{ZZ})$. These parameters are denoted hereafter as (f_{g2}, ϕ_{g2}) and (f_{g4}, ϕ_{g4}). The corresponding results are presented in Tables 11 and 12. To obtain these results, the effective cross sections $\sigma_{\rm SM}$, σ_{HVV} and σ_{AVV} of the HZZ interaction are calculated using the MG5 Monte Carlo generator [10] at Leading Order. The ratios of cross sections used in the calculation are: $\sigma_{HVV}/\sigma_{\rm SM} = 0.349$ and $\sigma_{AVV}/\sigma_{\rm SM} = 0.143$ respectively.

Appendix B

A nine-dimensional fit for the parameters $\tilde{\kappa}_{HVV}/\kappa_{\rm SM}$ and $(\tilde{\kappa}_{AVV}/\kappa_{\rm SM}) \cdot \tan\alpha$ using $H \to ZZ^* \to 4\ell$ decays is done to cross-check and validate the matrix element observable fit described in Section 6.3. The method implements a per-event likelihood that depends on nine discriminant observables: $m_{4\ell}$, $p_{T,4\ell}$, $\eta_{4\ell}$, $\cos\theta^*$, $\cos\theta_1$, $\cos\theta_2$, Φ, m_{12} and m_{34}. More information on these observables can be found in Section 5.4. A short description of the 9D fit method is included in Section 6.3. The expected and observed distributions of $-2\ln(\lambda)$ from the 9D fit are shown in Figure 11. These results are found to be consistent with the matrix element observable fit results shown in Figure 8.

Expected 95% CL limits			
$H \to WW^* \to e\nu\mu\nu$			
–	for $\phi_{g2} = 0$	and	$f_{g2} < 0.15$; $f_{g2} > 0.33$ for $\phi_{g2} = \pi$
–	for $\phi_{g4} = 0$	and	– for $\phi_{g4} = \pi$
$H \to ZZ^* \to 4\ell$			
$f_{g2} < 0.94$ for $\phi_{g2} = 0$		and	$f_{g2} < 0.16$ for $\phi_{g2} = \pi$
$f_{g4} < 0.56$ for $\phi_{g4} = 0$		and	$f_{g4} < 0.56$ for $\phi_{g4} = \pi$
Combination of $H \to ZZ^* \to 4\ell$ and $H \to WW^* \to e\nu\mu\nu$			
$f_{g2} < 0.89$ for $\phi_{g2} = 0$		and	$f_{g2} < 0.096$ for $\phi_{g2} = \pi$
$f_{g4} < 0.43$ for $\phi_{g4} = 0$		and	$f_{g4} < 0.44$ for $\phi_{g4} = \pi$

Table 11: Expected limits on (f_{g2}, ϕ_{g2}) and (f_{g4}, ϕ_{g4}) parameters defined in Ref. [6] obtained in the analyses of $H \to WW^* \to e\nu\mu\nu$ and $H \to ZZ^* \to 4\ell$ channels and for their combination. The symbol "–" denotes the absence of 95% CL sensitivity.

Observed 95% CL limits		
$H \to WW^* \to e\nu\mu\nu$		
$f_{g2} < 0.053$ for $\phi_{g2} = 0$	and	$f_{g2} < 0.20$; $0.26 < f_{g2} < 0.63$ for $\phi_{g2} = \pi$
$f_{g4} < 0.78$ for $\phi_{g4} = 0$	and	$f_{g4} < 0.84$ for $\phi_{g4} = \pi$
$H \to ZZ^* \to 4\ell$		
$f_{g2} < 0.68$ for $\phi_{g2} = 0$	and	$f_{g2} < 0.16$ for $\phi_{g2} = \pi$
$f_{g4} < 0.11$ for $\phi_{g4} = 0$	and	$f_{g4} < 0.54$ for $\phi_{g4} = \pi$
Combination of $H \to ZZ^* \to 4\ell$ and $H \to WW^* \to e\nu\mu\nu$		
$f_{g2} < 0.12$ for $\phi_{g2} = 0$	and	$f_{g2} < 0.16$ for $\phi_{g2} = \pi$
$f_{g4} < 0.090$ for $\phi_{g4} = 0$	and	$f_{g4} < 0.41$ for $\phi_{g4} = \pi$

Table 12: Observed imits on (f_{g2}, ϕ_{g2}) and (f_{g4}, ϕ_{g4}) parameters defined in Ref. [6] obtained in the analyses of $H \to WW^* \to e\nu\mu\nu$ and $H \to ZZ^* \to 4\ell$ channels and for their combination.

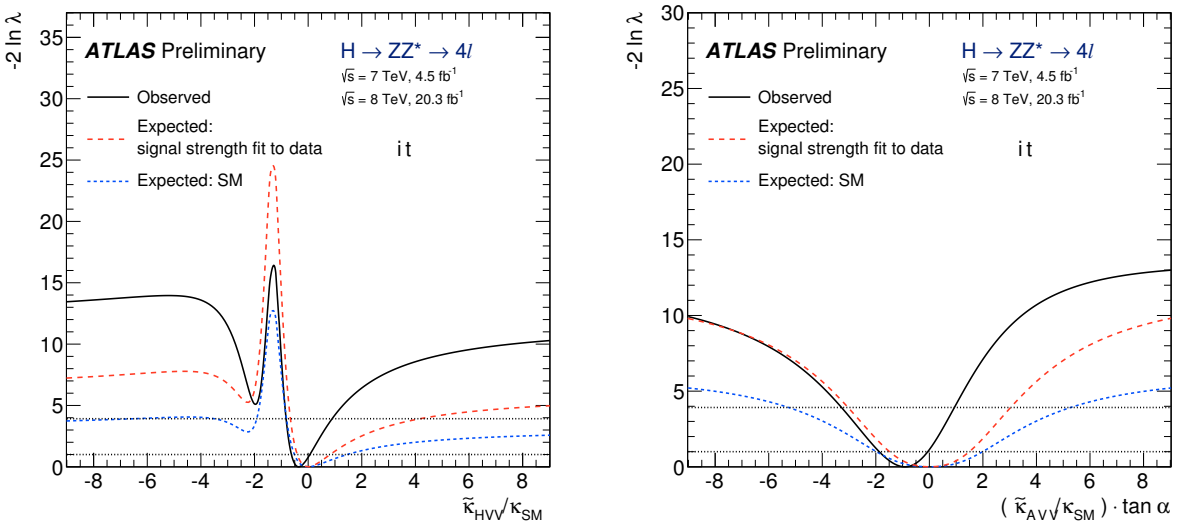

Figure 11: Expected and observed distributions of $-2\ln(\lambda)$ for fits of $\tilde{\kappa}_{HVV}/\kappa_{\rm SM}$ (left) and $(\tilde{\kappa}_{AVV}/\kappa_{\rm SM})\cdot\tan\alpha$ (right) for the $H \to ZZ^* \to 4\ell$ analysis using the cross-check 9D fit method. The expected curves are calculated assuming the Standard Model $J^P = 0^+$ with the signal strength $\mu = 1$ and with the signal strength fitted to data: $\hat{\mu}$. The horizontal dotted and dashed gray lines represent the levels of $-2\ln(\Lambda)$ above which the values of coupling ratios under study are excluded above 68 and 95% CL.

References

[1] ATLAS Collaboration, *Observation of a new particle in the search for the Standard Model Higgs boson with the ATLAS detector at the LHC*, Phys. Lett. B **716** (2012) 1, arXiv: 1207.7214 [hep-ex].

[2] CMS Collaboration, *Observation of a new boson at a mass of 125 GeV with the CMS experiment at the LHC*, Phys. Lett. B **716** (2012) 30, arXiv: 1207.7235 [hep-ex].

[3] ATLAS Collaboration, *Evidence for the spin-0 nature of the Higgs boson using ATLAS data*, Phys. Lett. **B726** (2013) 120–144, arXiv: 1307.1432 [hep-ex].

[4] CMS Collaboration, *Constraints on the spin-parity and anomalous HVV couplings of the Higgs boson in proton collisions at 7 and 8 TeV* (2014), arXiv: 1411.3441 [hep-ex].

[5] LHC Higgs Cross Section Working Group, *Handbook of LHC Higgs Cross Sections: 2. Differential Distributions*, CERN-2012-002 (2012), arXiv: 1201.3084 [hep-ph].

[6] LHC Higgs Cross Section Working Group, *Handbook of LHC Higgs Cross Sections: 3. Higgs Properties*, CERN-2013-004 (2013), arXiv: 1307.1347 [hep-ph].

[7] P. Artoisenet et al., *A framework for Higgs characterisation*, JHEP **1311** (2013) 043, arXiv: 1306.6464 [hep-ph].

[8] ATLAS Collaboration, *In Preparation: Determination of spin and parity properties of the Higgs boson*

in the $WW^* \to \ell\nu\ell\nu$ decay channel, HIGGS-2013-014 (2015), URL: https://cds.cern.ch/record/1968176.

[9] Y. e. a. Gao, *Spin determination of single-produced resonances at hadron colliders*, Phys. Rev. **D 81** (2010), arXiv: 1001.3396 [hep-ph].

[10] J. Alwall et al., *The automated computation of tree-level and next-to-leading order differential cross sections, and their matching to parton shower simulations*, JHEP **1407** (2014) 079, arXiv: 1405.0301 [hep-ph].

[11] ATLAS Collaboration, *The ATLAS Experiment at the CERN Large Hadron Collider*, JINST **3** (2008) S08003.

[12] L. D. Landau, *The moment of a 2-photon system*, Dokl. Akad. Nauk. **USSR 60** (1948) 207.

[13] C. N. Yang, *Selection Rules for the Dematerialization of a Particle Into Two Photons*, Phys. Rev. **77** (1950) 242.

[14] J. Beringer et al., *Particle Data Group*, Phys. Rev. **D 86** (2012) 010001.

[15] ATLAS Collaboration, *Measurements of fiducial and differential cross sections for Higgs boson production in the diphoton decay channel at $\sqrt{s}$ = 8 TeV with ATLAS*, JHEP **1409** (2014) 112, arXiv: 1407.4222 [hep-ex].

[16] ATLAS Collaboration, *Fiducial and differential cross sections of Higgs boson production measured in the four-lepton decay channel in pp collisions at $\sqrt{s}$=8 TeV with the ATLAS detector*, Phys.Lett. **B738** (2014) 234–253, arXiv: 1408.3226 [hep-ex].

[17] ATLAS Collaboration, *Measurements of Higgs boson production and couplings in the four-lepton channel in pp collisions at center-of-mass energies of 7 and 8 TeV with the ATLAS detector*, Phys.Rev. **D91**.1 (2015) 012006, arXiv: 1408.5191 [hep-ex].

[18] ATLAS Collaboration, *Observation and measurement of Higgs boson decays to WW^* with the ATLAS detector* (2014), arXiv: 1412.2641 [hep-ex].

[19] T. Sjostrand, S. Mrenna and P. Z. Skands, *A Brief Introduction to PYTHIA 8.1*, Comput. Phys. Commun. **178** (2008) 852, arXiv: 0710.3820 [hep-ph].

[20] ATLAS Collaboration, *The ATLAS Simulation Infrastructure*, Eur. Phys. J. **C 70** (2010) 823, arXiv: 1005.4568 [hep-ph].

[21] GEANT4 Collaboration, S. Agostinelli et al., *GEANT4: A simulation toolkit*, Nucl. Instrum. Meth. A **506** (2003) 250.

[22] ATLAS Collaboration, *The simulation principle and performance of the ATLAS fast calorimeter simulation FastCaloSim*, ATL-PHYS-PUB-2010-013, ATL-COM-PHYS-2010-838 (2010).

[23] S. Alioli et al., *NLO Higgs boson production via gluon fusion matched with shower in POWHEG*, J. High Energy Phys. **04** (2009) 002, arXiv: 0812.0578 [hep-ph].

[24] D. de Florian et al., *Transverse-momentum resummation: Higgs boson production at the Tevatron and the LHC*, J. High Energy Phys. **11** (2011) 064, For Higgs boson $p_T > m_H$, the calculation is switched from NLO+NLL to NLO, arXiv: 1109.2109 [hep-ph].

[25] M. Grazzini and H. Sargsyan, *Heavy-quark mass effects in Higgs boson production at the LHC*, J. High Energy Phys. **09** (2013) 129, arXiv: 1306.4581 [hep-ph].

[26] T. Sjostrand, S. Mrenna and P. Z. Skands, *PYTHIA 6.4 physics and manual*, J. High Energy Phys. **05** (2006) 026.

[27] S. Bolognesi et al., *On the spin and parity of a single-produced resonance at the LHC*, Phys. Rev. **D 86** (2012) 095031, arXiv: 1208.4018 [hep-ph].

[28] ATLAS Collaboration, *Measurement of Higgs boson production in the diphoton decay channel in pp collisions at center-of-mass energies of 7 and 8 TeV with the ATLAS detector* (2014), arxiv: hep-ex/1408.7084.

[29] G. Cowan et al., *Asymptotic formulae for likelihood-based tests of new physics*, Eur. Phys. J. **C71** (2011) 1554, arXiv: 1007.1727v2 [physics.data-an].

[30] A. L. Read, *Presentation of search results: The CL_s technique*, J. Phys. **G28** (2002) 2693.

[31] J. C. Collins and D. E. Soper, *Angular distribution of dileptons in high-energy hadron collisions*, Phys. Rev. **D 16** (7 1977) 2219.

[32] ATLAS Collaboration, *Measurement of the Higgs boson mass from the $H \to \gamma\gamma$ and $H \to ZZ^* \to 4\ell$ channels in pp collisions at center-of-mass energies of 7 and 8 TeV with the ATLAS detector*, Phys. Rev. D **90** (2014) 052004.

[33] L. Dixon and M. Siu, *Resonance continuum interference in the diphoton Higgs signal at the LHC*, Phys. Rev. Lett. **B90** (2003) 252001, arxiv: hep-ph/0302233.

[34] L. Dixon and Y. Li, *Bounding the Higgs Boson Width Through Interferometry*, Phys. Rev. Lett. **B111** (2013) 111802, arxiv: hep-ph/1305.3854.

[35] ATLAS Collaboration, *Measurement of the Higgs boson mass from the $H \to \gamma\gamma$ and $H \to ZZ^* \to 4e$ channels with the ATLAS detector at the LHC*, Phys. Lett. B **726** (2012) 1–29.

[36] ATLAS Collaboration, *Measurements of Higgs production and couplings using diboson final states with the ATLAS detector at the LHC*, Phys. Lett. B **726** (2012) 88–119.

[37] J. Alwall et al., *The automated computation of tree-level and next-to-leading order differential cross sections, and their matching to parton shower simulations*, J. High Energy Phys. **07** (2014) 079, arXiv: 1405.0301 [hep-ph].

[38] M. Diehl, O. Nachtmann and F. Nagel, *Triple gauge couplings in polarized $e^-e^+ \to W^-W^+$ and their measurement using optimal observables*, Eur.Phys.J. **C27** (2003) 375–397, arXiv: hep-ph/0209229 [hep-ph].

[39] M. Diehl and O. Nachtmann, *Optimal observables for measuring three gauge boson couplings in $e^+e^- \to W^+W^-$* (1996), arXiv: hep-ph/9603207 [hep-ph].